THE ASTROPHYSICAL JOURNAL, 401:226–245, 1992 December 10

HYDRODYNAMICAL EVOLUTION OF COALESCING BINARY NEUTRON STARS

FREDERIC A. RASIO[1] AND STUART L. SHAPIRO[2]
Center for Radiophysics and Space Research, Cornell University, Ithaca, NY 14853
Received 1991 December 23; accepted 1992 June 6

ABSTRACT

We report the results of three-dimensional Newtonian calculations of neutron-star binary coalescence using smooth particle hydrodynamics (SPH). Using a relaxation technique, we construct hydrostatic equilibrium models of close neutron-star binaries in synchronized circular orbits. We use a simple polytropic equation of state with $\Gamma = 2$ to represent cold nuclear matter, and we assume that the mass ratio $q = 1$, as observed in all known neutron-star binary systems. Using SPH, we study the dynamical stability of these hydrostatic equilibrium models. In a sequence of models with decreasing binary separation we find that dynamical instability sets in slightly before the point along the sequence where the surfaces of the two stars come into contact. This is in agreement with the known stability properties of the solutions of the classical Darwin problem for two identical, *incompressible* components. We find that the initial stage of the instability, consisting in the steady merging of the two stars into a single ellipsoidal object, is completed in about one orbital period. At this point sudden mass shedding is triggered, resulting in the rapid removal of matter from the central object through two outgoing spiral arms. This results in the rapid redistribution of matter in the system until a new, nearly axisymmetric, differentially rotating equilibrium structure has formed. Using the quadrupole approximation, we follow the emission of gravitational radiation from the onset of dynamical instability to the establishment of axial symmetry.

To support our results, we present several test-bed calculations which use SPH for binary systems. We consider axisymmetric, head-on collisions between two identical $\Gamma = 2$ polytropes and compare our SPH results to those of previous finite-difference calculations. Most importantly, we calculate solutions of the Roche and Darwin problems for polytropes with a wide range of adiabatic indices, $5/3 \leq \Gamma \leq 10$. We find good agreement with known analytical results, in both the nearly incompressible and highly compressible limiting regimes. These calculations provide stringent tests of our method's ability to hold stable binaries in equilibrium and to identify terminal points or the onset of dynamical instability along equilibrium sequences of close binaries. Such tests are crucial for establishing the credibility of numerical results and, in particular, of computed gravitational radiation waveforms.

Subject headings: binaries: close — hydrodynamics — radiation mechanisms: gravitational — stars: neutron

1. INTRODUCTION

Coalescing neutron-star binaries have long been recognized as one of the most promising sources of gravitational radiation (Dyson 1963; Clark & Eardley 1977; Clark, van den Heuvel, & Sutantyo 1979). Recently, interest in these sources has been revived with the design of laser interferometric gravitational-wave detectors: The Caltech-MIT LIGO project and its European counterparts (Abramovici et al. 1992; Schutz 1986, 1989; Thorne 1987; Vogt 1992). Indeed, these detectors are capable of making broad-band observations, and should be particularly sensitive to the radiation of frequency $\sim 10^2$–10^3 Hz emitted during the terminal phase of the coalescence.

Several neutron-star binaries have been observed in our Galaxy. The well-known binary pulsar PSR 1913 + 16 (Hulse & Taylor 1975) was the first to be discovered. Its orbital evolution, including relativistic effects, has now been observed for many years (Taylor & Weisberg 1989). In particular, the theoretical estimate for the gravitational-radiation decay rate of the orbit has been directly confirmed to high accuracy. The time it will take for the binary to complete its coalescence is estimated to be about 3×10^8 yr. Another similar system, PSR 2303+46, was discovered some years ago (Stokes, Taylor, & Dewey 1985), but its very long orbital period (about 12 days, compared to 8 hr for PSR 1913+16) has so far precluded the measurement of any relativistic effect. Recently, two more neutron-star binaries were found, both with short ~ 10 hr orbital periods: PSR 2127+11C in the globular cluster M15 (Anderson et al. 1990) and PSR 1534+12 (Wolszczan 1991), a high Galactic latitude nearby source. The coalescence times for these two new systems are about 2×10^8 and 3×10^9 yr, respectively.

Narayan, Piran, & Shemi (1991) and Phinney (1991) have used these latest observations to reevaluate the expected event rate of mergers, improving on earlier work by Clark et al. (1979) based solely on PSR 1913+16. In both of these recent studies the event rate is conservatively estimated to be about 3 per year within 200 Mpc. This rate could be much higher if there exists other types of neutron-star binaries which have so far escaped detection, such as those that could form in galactic nuclei containing clusters of stellar remnants (Quinlan & Shapiro 1989).

During most of the orbital evolution of a coalescing neutron-star binary, the separation between the two stars remains much larger than their radii, and hydrodynamic effects are completely negligible. In this regime, post-Newtonian perturbation methods can be used to calculate the evolution of the system, including the emission of gravitational radiation (Lincoln & Will 1990). Ultimately, however, as the binary

[1] Postal address: Institute for Advanced Study, Princeton, NJ 08540.
[2] Department of Physics and Department of Astronomy, Cornell University.

separation decreases, hydrodynamic effects will become more and more important. In particular, the characteristics of the final burst of gravitational radiation, emitted when the two stars finally merge together into a single object, will be determined entirely by hydrodynamics and will be very sensitive to the internal structure of the two stars.

Calculation of this final evolution is difficult, even in the Newtonian regime, because the evolution is strongly nonlinear and fully three-dimensional. In their pioneering work, Nakamura & Oohara (1989; see also Oohara & Nakamura 1989, 1990) have used a conventional, finite-difference hydrodynamics scheme to study the coalescence of two identical neutron stars represented by polytropes. They focused on the case in which the two stars result from the fission of a collapsing, rotating core. In this case the binary may never be in a state of hydrostatic equilibrium at any time during its evolution. By contrast, we use a Lagrangian method, smooth particle hydrodynamics, which is particularly well suited to three-dimensional problems, and we construct a true hydrostatic equilibrium model of a neutron-star binary as initial condition for our calculation.

We have made a considerable effort to check the ability of our code to hold stable binary configurations in dynamic equilibrium and to identify terminal points or the onset of instabilities along equilibrium sequences. Failure to pass these tests would result in spurious initial data, spurious fluid motions, and spurious gravitational wave amplitudes. We feel that such tests should be mandatory prerequisites for all numerical calculations of gravitational wave emission (see, e.g., Centrella et al. 1986, for a description of useful test-bed calculations).

The purpose of our work is to study in detail the hydrodynamics of the final merging of two neutron stars and the corresponding gravitational wave emission. In this paper, the first of a series, we focus our attention on a detailed description of our numerical method (§ 2) and a presentation of various test calculations, including the compressible Roche and Darwin problems (§ 3) and the head-on collision of two polytropes (§ 4). A complete coalescence calculation is presented (§ 5) for the simplest case of two identical neutron stars, represented by $\Gamma = 2$ polytropes, in a circular orbit, with their spins aligned and synchronized with the orbital rotation. In future papers, we will explore systematically the emission of gravitational radiation under less restrictive assumptions. Specifically, the effects of spin desynchronization or misalignment, eccentricity, and unequal masses will be studied, and more realistic equations of state, with varying stiffness, as well as the gravitational radiation reaction, will be introduced. In addition, thermal effects and neutrino diffusion will be incorporated, using a modified SPH scheme which we are presently developing (Lai, Rasio, & Shapiro 1992).

2. NUMERICAL METHOD

2.1. *Smooth Particle Hydrodynamics*

Smooth particle hydrodynamics (hereafter SPH) was introduced specifically to deal with astrophysical problems involving fluids moving arbitrarily in three dimensions. The key idea is to calculate the pressure gradient forces by kernel estimation, directly from the particle positions, rather than by finite differencing on a grid, as is done in more traditional Lagrangian methods such as PIC (the particle-in-cell method; see, e.g., Harlow 1988). This idea was originally introduced by Lucy (1977) and Gingold & Monaghan (1977), who applied it to the calculation of dynamical fission instabilities in rapidly rotating stars. Since then, a wide variety of astrophysical problems have been tackled using SPH. In the past few years, these have included galaxy formation (Evrard 1988; Shapiro, Kang, & Villumsen 1990), star formation (Monaghan & Lattanzio 1991), supernova explosions (Nagasawa, Nakamura, & Miyama 1988; Herant & Benz 1991), solar system formation (Boss, Cameron, & Benz 1992), tidal disruption of stars by massive black holes (Evans & Kochanek 1989), and stellar collisions (Davies & Benz 1991; Rasio & Shapiro 1991). The method itself has also undergone major advances. Most notably, artificial viscosity has been incorporated (Lattanzio et al. 1986), as well as powerful algorithms for the calculation of self-gravity, such as particle-mesh methods (Evrard 1988) and tree algorithms (Hernquist & Katz 1989; Benz et al. 1990).

In SPH we must solve the equations of motion of a large number N of Langrangian fluid particles,

$$\dot{\boldsymbol{x}}_i = \boldsymbol{v}_i \,,$$
$$m_i \dot{\boldsymbol{v}}_i = \boldsymbol{F}_i^{(\mathrm{Grav})} + \boldsymbol{F}_i^{(\mathrm{Hydro})} \,. \tag{1}$$

The fluid density at $\boldsymbol{x}_i$ is estimated from the masses and positions of neighboring particles as a local weighted average,

$$\rho_i = \sum_j m_j W_{ij} \,. \tag{2}$$

We use symmetric weights, $W_{ij} = W_{ji}$, calculated following the method of Hernquist & Katz (1989) as

$$W_{ij} = \tfrac{1}{2}[W(|\boldsymbol{r}_i - \boldsymbol{r}_j|, h_i) + W(|\boldsymbol{r}_i - \boldsymbol{r}_j|, h_j)] \,. \tag{3}$$

Here h_i is a smoothing length associated with particle i, and $W(r, h)$ is an interpolation kernel, for which we use the second-order accurate form of Monaghan & Lattanzio (1985),

$$W(r, h) = \frac{1}{\pi h^3} \begin{cases} 1 - \frac{3}{2}\left(\frac{r}{h}\right)^2 + \frac{3}{4}\left(\frac{r}{h}\right)^3 \,, & 0 \le \frac{r}{h} < 1 \,, \\ \frac{1}{4}\left[2 - \left(\frac{r}{h}\right)\right]^3 \,, & 1 \le \frac{r}{h} < 2 \,, \\ 0 \,, & \frac{r}{h} \ge 2 \,. \end{cases} \tag{4}$$

When the true density $\rho(\boldsymbol{x})$ of the fluid is represented by an appropriate distribution of particle positions, masses, and smoothing lengths, one can show that $\rho_i = \rho(\boldsymbol{x}_i) + O(h_i^2)$ (see, e.g., Monaghan 1985). Since our calculations assume an adiabatic equation of state for the gas, the pressure at $\boldsymbol{x}_i$ will be estimated as

$$P_i = A_i \rho_i^{\Gamma} \,, \tag{5}$$

where A_i is a function of the specific entropy at $\boldsymbol{x}_i$, and Γ is the constant ratio of specific heats. The local speed of sound is $c_i = (\Gamma P_i/\rho_i)^{1/2}$. Throughout this paper, we assume that the value of Γ defining an initial polytropic equilibrium and the value associated with subsequent adiabatic changes are identical.

The hydrodynamical part of the force on particle i is calculated as

$$\boldsymbol{F}_i^{(\mathrm{Hydro})} = -\sum_j m_i m_j \left[\left(\frac{p_i}{\rho_i^2} + \frac{p_j}{\rho_j^2}\right) + \Pi_{ij}\right] \nabla_i W_{ij} \,. \tag{6}$$

Here Π_{ij} is an artificial viscosity term, while the rest of the above expression represents one of many possible SPH-estimators for the local pressure gradient force $-(\nabla p/\rho)_i$ (see, e.g., Monaghan 1985). This form has the advantage of being computationally convenient, while at the same time providing a natural set of conservation laws (see below). For the artificial viscosity we adopt a symmetrized version of the form proposed by Monaghan (1989):

$$\Pi_{ij} = \frac{-\alpha\mu_{ij}c_{ij} + \beta\mu_{ij}^2}{\rho_{ij}}, \tag{7}$$

where $\rho_{ij} = (\rho_i + \rho_j)/2$, $c_{ij} = (c_i + c_j)/2$, and

$$\mu_{ij} = \begin{cases} \dfrac{(\boldsymbol{v}_i - \boldsymbol{v}_j)\cdot(\boldsymbol{r}_i - \boldsymbol{r}_j)}{h_{ij}(|\boldsymbol{r}_i - \boldsymbol{r}_j|^2/h_{ij}^2 + \eta^2)}, & \text{when } (\boldsymbol{v}_i - \boldsymbol{v}_j)\cdot(\boldsymbol{r}_i - \boldsymbol{r}_j) < 0, \\ 0, & \text{when } (\boldsymbol{v}_i - \boldsymbol{v}_j)\cdot(\boldsymbol{r}_i - \boldsymbol{r}_j) \geq 0, \end{cases} \tag{8}$$

with $h_{ij} = (h_i + h_j)/2$. This represents a combination of the usual von Neuman-Richtmyer artificial viscosity and a bulk viscosity. It provides a good description of shocks when the constants satisfy $\alpha \approx \beta \approx 2$, and $\eta^2 \sim 10^{-2}$ (Monaghan 1989; Hernquist & Katz 1989). To complete the description of the fluid, we write the first law of thermodynamics at $\boldsymbol{x}_i$ as

$$\frac{dA_i}{dt} = \frac{\Gamma - 1}{2\rho_i^{\Gamma-1}} \sum_j m_j \Pi_{ij}(\boldsymbol{v}_i - \boldsymbol{v}_j)\cdot\nabla_i W_{ij}. \tag{9}$$

The set of equations (1)–(9) has the important property of guaranteeing, at least in the absence of gravity, the *exact* conservation of momentum and energy. We define the *total momentum* of the fluid as

$$\boldsymbol{P}_{\rm tot} \equiv \sum_i m_i \boldsymbol{v}_i, \tag{10}$$

and the *total energy* of the fluid as

$$\epsilon_{\rm tot} \equiv \sum_i \left(\frac{m_i}{2} v_i^2 + m_i u_i\right), \tag{11}$$

where u_i is the *specific internal energy* of a fluid particle,

$$u_i = \frac{p_i}{(\gamma - 1)\rho_i} = \frac{A_i}{\gamma - 1}\rho_i^{\gamma-1}. \tag{12}$$

Given these definitions, one can show (Rasio 1991) that equations (1)–(9), with a symmetric kernel and h_i = constant, imply $d\boldsymbol{P}_{\rm tot}/dt \equiv 0$ and $d\epsilon_{\rm tot}/dt \equiv 0$. Similarly, if we define the *total entropy* of the system by

$$S_{\rm tot} = \frac{k_{\rm B}}{(\Gamma - 1)\mu} \sum_i m_i \ln\left(\frac{A_i}{\Gamma - 1}\right) + S_0, \tag{13}$$

we see from equation (9) that $dS_{\rm tot}/dt \equiv 0$ in the absence of shocks. Here $k_{\rm B}$ is Boltzmann's constant, μ is the mean molecular weight, and S_0 is an arbitrary constant, so that equation (13) reduces to the usual thermodynamic definition of the entropy for an ideal gas.

An evolution equation for u_i, rather that A_i, has often been used in other implementations of SPH (see, e.g., Hernquist & Katz 1989; Rasio & Shapiro 1991). We find that the use of equation (9) has several practical advantages. First, when the artificial viscosity is not used, or, if it is used, for those fluid particles away from shocks for which $\Pi_{ij} = 0$, the property that A_i = constant can be used directly so that no time is wasted integrating an additional equation. But most importantly, the numerical results obtained by integrating equation (9) are often more accurate than those obtained with an energy equation. This can be understood as follows. Since the kernel $W(r, h)$ is a monotonically decreasing function of r, the right-hand side of equation (9) is *positive definite*, because $\Pi_{ij} > 0$ when $(\boldsymbol{v}_i - \boldsymbol{v}_j)\cdot(\boldsymbol{x}_i - \boldsymbol{x}_j) < 0$ and is zero otherwise. This property guarantees that the integration of equation (9) will lead to physically reasonable results, with the entropy never decreasing in time. In contrast, nothing guarantees that the numerical integration of the energy equation will preserve the positivity of u_i. This can sometimes lead to unacceptably large errors. Consider for example the nearly complete adiabatic expansion of a region of the fluid into the vacuum. Particles in that region will have $u_i \to 0$ at late times. Inevitably, numerical truncation errors will lead to u_i being set equal to zero (or worse, $u_i < 0$) for some of these particles. This is not in itself a problem, since the contribution from those particles to the total internal energy of the fluid is indeed negligible. However, the specific entropy associated with $A_i = (\Gamma - 1)u_i/\rho_i^{\Gamma-1}$ has also vanished in the process, even though it may not be negligible at all. Since A_i is normally a conserved quantity, the system will keep forever the memory of this error, and the solution could become meaningless if, for example, that particle were to return later to a more active interior region.

One *disadvantage* of using the entropy equation is that when time-dependent smoothing lengths are introduced, this can lead to errors in the conservation of total energy. These errors are directly related to the level of *numerical noise* in the system, measured by the ratio σ/c of the velocity dispersion of random particle motions to the local speed of sound. Consider a small region of fluid where all particles have smoothing lengths $h_i = h(t)$, One can show on the basis of statistical mechanics arguments (Rasio 1991), and verify empirically, that the total fluid energy $\epsilon_{\rm tot}$ in that region will evolve, as a result of the time-dependent h, according to the following approximate relation,

$$\left\langle \frac{1}{\epsilon_{\rm tot}} \frac{d\epsilon_{\rm tot}}{dt} \right\rangle \approx -3\Gamma(\Gamma - 1)\left(\frac{1}{h}\frac{dh}{dt}\right)\frac{\sigma^2}{c^2}, \tag{14}$$

where the angle bracket denotes an ensemble averaging.

In practice, the use of time-dependent, individual particle smoothing lengths h_i is essential in ensuring that the spatial resolution remains acceptable throughout a calculation. The local values of h_i must continually adapt themselves to expanding and contracting regions of the fluid. The convenient prescription that we use is to continually update the values of h_i so that the *number of neighbors*, N_N, of any particle remains approximately constant in time. This number is a very important parameter in the calculation. It is directly related to the level of numerical noise in the system. In general, we find that, for given physical conditions, the noise level in a calculation always decreases when N_N is increased. Moreover, higher *accuracy* is obtained in SPH calculations only when *both* the number of particles N *and* the number of neighbors N_N are increased, with N increasing faster than N_N so that the smoothing lengths h_i decrease (Rasio 1991). The choice of the parameter N_N for a given calculation will therefore be dictated by a compromise between what is considered an acceptable level of numerical noise and the desired spatial resolution (which is $\approx h \propto 1/N_N^{1/d}$ in d dimensions). For most three-dimensional calculations with $N \sim 10^4$, we have found that $N_N \gtrsim 64$ is an adequate choice.

To provide reasonable accuracy, the SPH method requires

the use of very large numbers of particles (typically $N \gg 1000$). This rules out a direct summation method for calculating the gravitational field of the system. Instead, we have turned to a grid-based method for calculating the gravitational field of the fluid. The SPH definition of the (smooth) density (eq. [2]) is used to calculate the values of the source term for the Poisson equation at grid points. An FFT-based convolution algorithm (Hockney & Eastwood 1988; Wells et al. 1990) is used to solve for the gravitational potential on the grid. Forces at grid points are obtained by finite differencing, and then interpolated onto the particle positions. For the problem described in this paper, the use of a grid is further motivated by our intention to incorporate into a future version of our numerical code the calculation of post-Newtonian effects, such as the gravitational radiation reaction, which can only be done by finite-differencing. In our code, we also perform the neighbor searching using a grid-based algorithm. Specifically, we use a variant of the method usually adopted in P^3M particle codes (Hockney & Eastwood 1988). This method is extremely efficient, even for wide distributions of smoothing lengths, provided that one is careful to fine-tune the ratio $L/\langle h_i \rangle$ of the grid separation L to the average particle smoothing length $\langle h_i \rangle$.

The time-evolution equations (1) are integrated using an explicit leap-frog scheme. This provides second-order accuracy in time. Note that such a low-order scheme is appropriate here because pressure gradient forces are subject to numerical noise. For stability, the time step must satisfy a Courant condition with h_i replacing the usual grid separation. For accuracy, the time step must also be a small enough fraction of the system's dynamical time. In practice we calculate the time step as in Monaghan (1989), setting $\Delta t = \mathrm{Min}(\Delta t_1, \Delta t_2)$ with

$$\Delta t_1 = k\ \mathrm{Min}_i\left(\frac{h_i}{c_i + 1.2\alpha c_i + 1.2\beta\ \mathrm{Max}_j \mu_{ij}}\right), \tag{15}$$

where $k \approx 0.1$, and $\Delta t_2 = \mathrm{Min}_i(h_i/\dot{v}_i)^{1/2}$.

2.1. *The Quadrupole Formula in SPH*

For nearly-Newtonian fluids, the emission of gravitational waves can be calculated using the quadrupole approximation (see, e.g., Misner, Thorne, & Wheeler 1970). In this approximation, the amplitude h_{lm}^{TT} of the wave in the transverse-traceless gauge can be written

$$h_{lm}^{\mathrm{TT}} = \frac{2}{r}\frac{G}{c^4}\frac{d^2 I_{lm}^{\mathrm{TT}}(t-r)}{dt^2}. \tag{16}$$

Here I_{lm}^{TT} is the transverse-traceless part of the reduced quadrupole moment, i.e.,

$$I_{lm}^{\mathrm{TT}} = P_{lk} I_{kn} P_{nm} - \tfrac{1}{2} P_{lm} P_{kn} I_{kn}, \tag{17}$$

where $P_{kl} = \delta_{kl} - n_k n_l$ is the projection operator onto the plane transverse to the radial direction $n_k = x_k/r$,

$$I_{lm} = I_{lm} - \tfrac{1}{3}\delta_{lm} I \tag{18}$$

is the reduced quadrupole moment, and

$$I_{lm} = \int \rho x_l x_m\, d\boldsymbol{x}. \tag{19}$$

The total power crossing a distant sphere of radius r at retarded time t is

$$\left(\frac{d\epsilon}{dt}\right)_{\mathrm{GW}} = \frac{1}{5}\frac{G}{c^5}\left\langle \frac{d^3 I_{lm}}{dt^3}\frac{d^3 I_{lm}}{dt^3}\right\rangle, \tag{20}$$

while the total angular momentum carried off by gravitational waves is

$$\left(\frac{dJ_k}{dt}\right)_{\mathrm{GW}} = \frac{2}{5}\frac{G}{c^5}\epsilon_{klm}\left\langle \frac{d^2 I_{ln}}{dt^2}\frac{d^3 I_{mn}}{dt^3}\right\rangle. \tag{21}$$

In the orthonormal basis defined by

$$\boldsymbol{e}_{\hat{r}} = \frac{\partial}{\partial r}, \quad \boldsymbol{e}_{\hat{\theta}} = \frac{1}{r}\frac{\partial}{\partial \theta}, \quad \boldsymbol{e}_{\hat{\phi}} = \frac{1}{r\sin\theta}\frac{\partial}{\partial \phi}, \tag{22}$$

the two basis tensors for transverse-traceless tensors corresponding to a propagation along $\boldsymbol{e}_{\hat{r}}$ are

$$\begin{aligned} \boldsymbol{e}_+ &= \boldsymbol{e}_{\hat{\theta}} \otimes \boldsymbol{e}_{\hat{\theta}} - \boldsymbol{e}_{\hat{\phi}} \otimes \boldsymbol{e}_{\hat{\phi}}, \\ \boldsymbol{e}_\times &= \boldsymbol{e}_{\hat{\theta}} \otimes \boldsymbol{e}_{\hat{\phi}} + \boldsymbol{e}_{\hat{\phi}} \otimes \boldsymbol{e}_{\hat{\theta}}. \end{aligned} \tag{23}$$

From equations (16) and (17) with $\boldsymbol{n} = \boldsymbol{e}_{\hat{r}}$ we find

$$r\boldsymbol{h}^{\mathrm{TT}} = (\ddot{I}_{\hat{\theta}\hat{\theta}} - \ddot{I}_{\hat{\phi}\hat{\phi}})\boldsymbol{e}_+ + 2\ddot{I}_{\hat{\theta}\hat{\phi}}\boldsymbol{e}_\times, \tag{24}$$

where the components in spherical coordinates are related to the Cartesian components by (see, e.g., Kochanek et al. 1990)

$$\begin{aligned} \ddot{I}_{\hat{\theta}\hat{\theta}} &= (\ddot{I}_{xx}\cos^2\phi + \ddot{I}_{yy}\sin^2\phi + \ddot{I}_{xy}\sin 2\phi)\cos^2\theta \\ &\quad + \ddot{I}_{zz}\sin^2\theta - (\ddot{I}_{xz}\cos\phi + \ddot{I}_{yz}\sin\phi)\sin 2\theta, \\ \ddot{I}_{\hat{\phi}\hat{\phi}} &= \ddot{I}_{xx}\sin^2\phi + \ddot{I}_{yy}\cos^2\phi - \ddot{I}_{xy}\sin 2\phi, \\ \ddot{I}_{\hat{\theta}\hat{\phi}} &= -\tfrac{1}{2}(\ddot{I}_{xx} - \ddot{I}_{yy})\cos\theta\sin 2\phi + \ddot{I}_{xy}\cos\theta\cos 2\phi \\ &\quad + (\ddot{I}_{xz}\sin\phi - \ddot{I}_{yz}\cos\phi)\sin\theta. \end{aligned} \tag{25}$$

For a perfect fluid, the first and second time derivatives of the quadrupole tensor can be evaluated directly using the method of Finn (1989). We use the continuity equation to write the first time derivative of equation (19) as

$$\dot{I}_{lm} = -\int \nabla\cdot(\rho\boldsymbol{v}) x_l x_m\, d\boldsymbol{x}. \tag{26}$$

Integrating by parts then gives

$$\dot{I}_{lm} = \int \rho(v_l x_m + v_m x_l)\, d\boldsymbol{x}. \tag{27}$$

Similarly, taking the time derivative of equation (27) and using both the continuity equation and the Euler equation of motion we get

$$\begin{aligned} \ddot{I}_{lm} = -\int\Big[&\nabla\cdot(\rho\boldsymbol{v})(v_l x_m + v_m x_l) \\ &+ \rho x_m\left(\frac{1}{\rho}\partial_l P + \partial_l\Phi + v^k\partial_k v_l\right) \\ &+ \rho x_l\left(\frac{1}{\rho}\partial_m P + \partial_m\Phi + v^k\partial_k v_m\right)\Big] d^3x, \end{aligned} \tag{28}$$

where Φ is the Newtonian gravitational potential. After integration by parts and simplification this gives

$$\ddot{I}_{lm} = \int[2\rho v_l v_m + 2P\delta_{lm} - \rho(x_m\partial_l\Phi + x_l\partial_m\Phi)]\, d\boldsymbol{x}. \tag{29}$$

In SPH, we replace the integration in equation (29) by a sum over all particles, so that

$$\begin{aligned} \ddot{I}_{lm}^{(\mathrm{SPH})} = &\sum_{i=1}^{N} m^{(i)} \\ &\times\left[2v_l^{(i)}v_m^{(i)} + 2\frac{P^{(i)}}{\rho^{(i)}}\delta_{lm} + (x_m^{(i)}g_l^{(i)} + x_l^{(i)}g_m^{(i)})\right]. \end{aligned} \tag{30}$$

Here, to avoid confusion, an upperscript (i) has been used to represent the particle index, and $\boldsymbol{g}^{(i)}$ is the gravitational force at $\boldsymbol{x}^{(i)}$. Equations (24), (25), and (30) allow us to calculate the gravitational wave amplitude directly from particle positions and velocities, without the need to perform numerical differentiations. One numerical differentiation is required, however, to calculate the total power and angular momentum carried away by the waves from equations (20) and (21).

3. CONSTRUCTION OF HYDROSTATIC EQUILIBRIUM MODELS

3.1. *Introduction*

Until very recently, calculations of hydrostatic equilibrium models for close binary stars could only be performed with approximate perturbation methods. This is because the problem is intrinsically three-dimensional: even for the simplest systems, where the spins of both components are parallel to the orbital angular momentum and synchronized with the orbital motion, the axisymmetry of the rotation is broken by the presence of tidal forces, which have a symmetry axis perpendicular to the rotation axis.

For *incompressible configurations*, the tensor virial method has been used with great success to study analytically the linear departures from spherical symmetry (cf. Chandrasekhar 1969, and references therein). Unfortunately, when the binary separation is small, the linear approximation breaks down, and the method no longer gives accurate results, especially near the surface of the two components.

For *highly compressible configurations* (in practice, polytropes with indices $n \geq 3$, or $\Gamma \leq 4/3$), the first-order perturbation technique of Monaghan & Roxburgh (1965) has been used for the equilibrium structure (Martin 1970; Naylor & Anand 1970). In this technique, the polytrope is divided into two regions. In the inner region, the perturbing forces are assumed to be small and a linear perturbation of the Lane-Emden solution is used. In the outer region, the density is assumed to be negligible so that the potential can be written as a solution of the Laplace equation. The two solutions are then matched at some critical radius. This method does not break down when the surface deformations become very nonlinear, but is only applicable to highly compressible, centrally condensed stars for which the two-region approximation is valid.

Little is known about the intermediate case of mildly incompressible ($\Gamma \gtrsim 5/3$) components with large, nonlinear surface deformations. Close binary neutron stars belong precisely to this category. In this section, we show how SPH can be used to construct hydrostatic equilibrium models of binary stars with *arbitrarily large surface deformations*, and *arbitrarily stiff equations of state*. Specifically, models can be constructed where the surfaces of the two components are in contact, and adiabatic indices as high as $\Gamma = 10$ can be used with no particular problem. In § 3.2, we demonstrate the accuracy of the method by calculating solutions of the classical Roche problem, which has known semi-analytical solutions. The deformation of more compressible stars (polytropes) by point mass companions is also examined, and the SPH results are compared to approximate analytical solutions valid in the "highly compressible" limit (§ 3.3). Finally, in § 3.4, we construct models of binaries containing two polytropes of equal masses with various adiabatic indices. In particular, binaries containing two identical polytropes with $\Gamma = 2$ are constructed to model neutron star binaries.

3.2. *The Classical Roche Problem*

The classical Roche problem consists in determining the equilibrium structure of a homogeneous, incompressible body (called the primary), rigidly rotating about a point mass companion (called the secondary). The perturbing potential due to rotation and tidal effects is expanded in series of the coordinates about the center of mass of the primary, and only the lowest order (quadratic) terms are retained. Given these simplifications, the potential surfaces are ellipsoidal and a complete solution can be found semi-analytically.

We adopt notations and conventions similar to those of Chandrasekhar (1969). The origin of the coordinate system is at the center of mass of the primary (mass M). The x-axis is the axis of the binary, going from the primary to the secondary (mass M'). The z-axis is parallel to the rotation axis. The orbital angular frequency Ω is given by Kepler's third law, which we write as

$$\Omega^2 = \frac{G(M + M')}{a^3} = \mu(1 + q) , \tag{31}$$

where a is the binary separation, $q \equiv M/M'$ is the mass ratio, and $\mu \equiv GM'/a^3$ is a measure of the strength of the tidal forces. In terms of these quantities the perturbation potential can be written (cf. Chandrasekhar 1969, chap. 8, eq. [6])

$$\Phi^{(\text{Roche})} = \tfrac{1}{2}\Omega^2(x^2 + y^2) + \mu(x^2 - \tfrac{1}{2}y^2 - \tfrac{1}{2}z^2) . \tag{32}$$

Terms of higher order than quadratic in the coordinates have been neglected in this expression. The coefficient of the linear term vanishes identically when Ω satisifes equation (31).

Numerically, we solve the problem by a *relaxation technique*. First, we construct a spherical, unperturbed model of the primary. We cannot deal directly with incompressible matter in SPH, but we can solve the problem for polytropes with increasingly large values of Γ and treat the incompressible case as the $\Gamma \to \infty$ limit.

The SPH model of the unperturbed polytrope is constructed as follows. We place $N \approx 4 \times 10^4$ particles at the points of a cubic lattice in a sphere of radius R. Individual particle masses $m_i = \rho(r_i)/n$ are assigned, where $n = N/(4\pi R^3/3)$ is the (uniform) number density of particles and $\rho(r_i)$ is the exact density at r_i, determined by solving the Lane-Emden equation. Such a uniform distribution of particles ensures that the spatial resolution remains good near the surface of the star, where the deformations are largest. The entropy variables A_i of all particles are given the (constant) value of P/ρ^Γ for the polytrope. Since the spatial distribution of particles is homogeneous, a constant number of neighbors $N_N \approx 100$ for all particles is easily achieved by setting $h_i = \text{constant} = (1/2)[3N_N/(4\pi n)]^{1/2}$.

An external perturbation force, derived from the potential (32), is then applied to the polytrope. Specifically, we use the following equations of motion:

$$\frac{d\boldsymbol{v}_i}{dt} = \boldsymbol{F}_i^{(\text{Hydro})} + \boldsymbol{F}_i^{(\text{Grav})} + \boldsymbol{F}_i^{(\text{Roche})} - \frac{\boldsymbol{v}_i}{t_{\text{relax}}} , \tag{33}$$

where $\boldsymbol{F}_i^{(\text{Hydro})}$ is the pressure gradient force of equation (6) and $\boldsymbol{F}_i^{(\text{Grav})}$ represents the *self-gravity* of the primary. The external force for the Roche problem is obtained from equation (32) as

$$\boldsymbol{F}_i^{(\text{Roche})} = \nabla\Phi^{(\text{Roche})} = \mu(3 + q)x_i\hat{\boldsymbol{x}} + \mu q y_i\hat{\boldsymbol{y}} - \mu z_i\hat{\boldsymbol{z}} . \tag{34}$$

A linear friction term has also been added in equation (33) to

guarantee that an equilibrium is reached at the end of the calculation. In the absence of such a friction term, the sudden application of the external force $F^{(\mathrm{Roche})}$ would result in oscillations of the fluid about the new equilibrium configuration. It is important to choose the relaxation time t_{relax} in such a way that the damping of these oscillations is *slightly overcritical*. This implies $t_{\mathrm{relax}} \lesssim t_{\mathrm{osc}}$, where $t_{\mathrm{osc}} \sim (G\rho)^{-1/2}$ is a typical oscillation period. If the relaxation time is longer than critical, "Roche lobe overflow" can occur near a critical solution, the star losing some mass before an equilibrium is reached. On the other hand, if the relaxation time is too short, the equilibrium is reached much more slowly and computational resources are wasted.

We now describe our numerical results. For simplicity, we only consider the equal mass case, where $q = 1$. The units we use are such that $G = M = R = 1$, where R is the radius of the *unperturbed* polytrope. (Note that, in this paper, we will use geometrized units, where $G = c = 1$, only when describing gravitational radiation.) For each of three values of the adiabatic index, $\Gamma = 5/3$, 2, and 10, we have constructed a sequence of about 10 equilibrium models with increasing values of μ. Of particular interest is the location along each sequence of the *critical configuration*, beyond which no equilibrium solution of the Roche problem exists.

Two simple methods can be used to locate the critical point along a sequence. The easiest but least sensitive method is simply to follow the time evolution of some quantity measuring the departure from spherical symmetry and to look for a divergent behavior. This is illustrated in Figure 1, which shows the evolution of the maximum elongation along the axis of the binary for four different calculations with $\Gamma = 2$. We used this method to obtain a first, coarse determination of μ_{crit}. A more accurate determination of μ_{crit} using this method would require prohibitively long calculations, since the growth time of the deformation can be very long near the critical point. A more sensitive method, which we used to refine our search, consists in looking for early signs of mass shedding, or "overflow" near the axis. This is illustrated in Figure 2, which shows contour lines of the density in the orbital plane for various models with $\Gamma = 2$ near the critical solution. The scale is linear and the outermost contour corresponds to $\rho = 0$. The first signs of overflow are clearly apparent for $\mu = 0.070$.

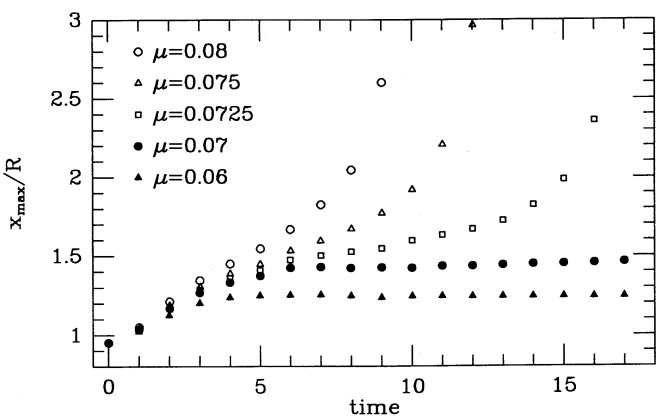

FIG. 1.—Time evolution of the maximum elongation x_{max}/R of the primary along the axis of the binary, for four different models along the $\Gamma = 2$ compressible Roche sequence. Time is units of $(R^3/GM)^{1/2}$. The critical point is clearly located at $\mu \approx 0.07$.

TABLE 1

PROPERTIES OF THE CRITICAL SOLUTIONS IN THE COMPRESSIBLE ROCHE PROBLEM

Γ	μ_{crit}	x_{crit}/R
1.2	0.074	1.50
5/3	0.074	1.46
2	0.069	1.58
10	0.058	1.58
∞	0.053	1.56

Table 1 summarizes the properties of the critical configurations for various values of Γ. The values listed under $\Gamma = \infty$ are from Chandrasekhar (1969). Those listed under $\Gamma = 1.2$ (corresponding to the "infinitely compressible" $n = 5$ polytrope) are from the approximate solution described below in § 3.3. We find that the SPH result $\mu_{\mathrm{crit}} = 0.058$ for $\gamma = 10$ is very close to, though slightly larger than, the value $\mu_{\mathrm{crit}} = 0.053$ given by Chandrasekhar (1969, chap. 8, Table XVIII).[3]. As expected, the value of μ_{crit} increases for decreasing Γ, the more centrally condensed structures being less sensitive to tidal forces. The interior profiles of the various critical configurations are compared in Figure 3.

3.3. *The Compressible Roche Problem*

For small Γ, the SPH results for the Roche problem should be compared to those obtained by the method of Monaghan & Roxburgh (1965) for the perturbation of centrally condensed polytropes (cf. § 3.1). Unfortunately, as far as we know, no calculation of the Roche problem based on this method has been published. However, we can easily obtain some analytic results for the profiles *near the surface* of the primary. Indeed, for a centrally condensed structure, we know that the gravitational potential of the primary can be approximated as $-GM/r$ near its surface. Therefore the structure of the primary near its surface can be determined approximately by solving the hydrostatic equilibrium equation,

$$\frac{1}{\rho}\nabla(A\rho^{\Gamma}) + \nabla\Phi = 0\,, \tag{35}$$

where the potential Φ is a known function (cf. eq. [32]),

$$\Phi = -\frac{GM}{r} - \frac{1}{2}\Omega^2(x^2 + y^2) - \mu\left(x^2 - \frac{1}{2}y^2 - \frac{1}{2}z^2\right). \tag{36}$$

The solution of equation (35) can immediately be written as $H + \Phi = \Phi_0$, where Φ_0 is a constant and H is the enthalpy,

$$H = \int \frac{dP}{\rho} = \frac{\Gamma}{\Gamma - 1} A\rho^{\Gamma - 1}\,. \tag{37}$$

Solving for the density we get

$$\rho = \left[\frac{(\Gamma - 1)}{\Gamma A}(\Phi_0 - \Phi)\right]^{1/(\Gamma - 1)}. \tag{38}$$

The constant Φ_0 in equation (38) is clearly the value of the potential at the surface (where $\rho = 0$). In the method of Monaghan & Roxburgh (1965), the value of Φ_0 is determined by matching the exterior solution, equation (38), to an interior

[3] Note that μ_{max} in Chandrasekhar (1969) is given in the unit $\pi G\bar{\rho}$. Since $G = 1$ and $\bar{\rho} = 3/(4\pi)$ in our units, we have μ_{crit} (here) $= 0.75 \times \mu_{\mathrm{max}}$ (Chandrasekhar).

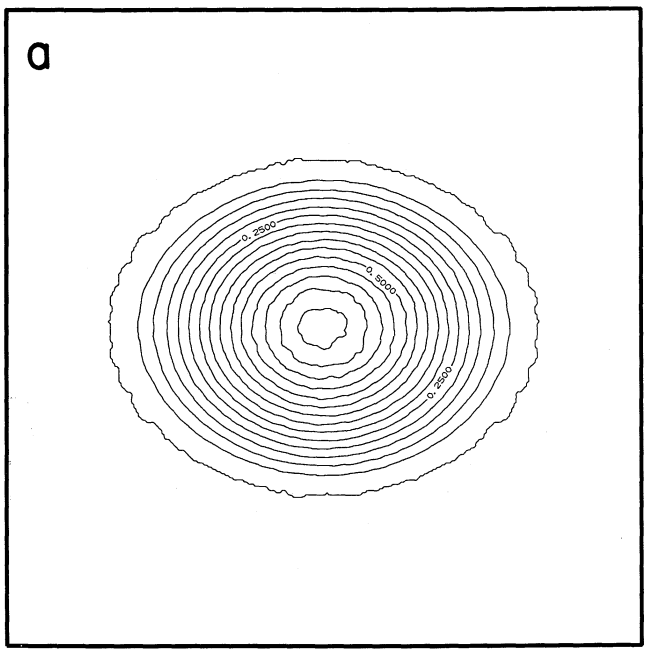

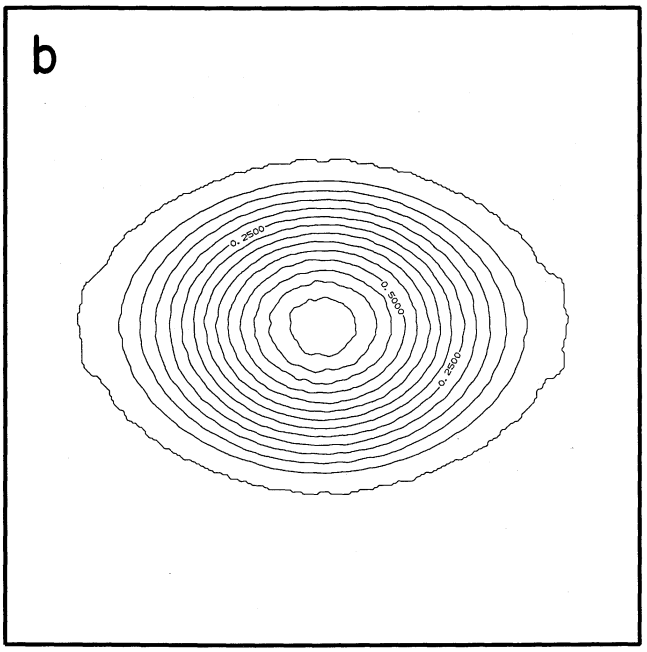

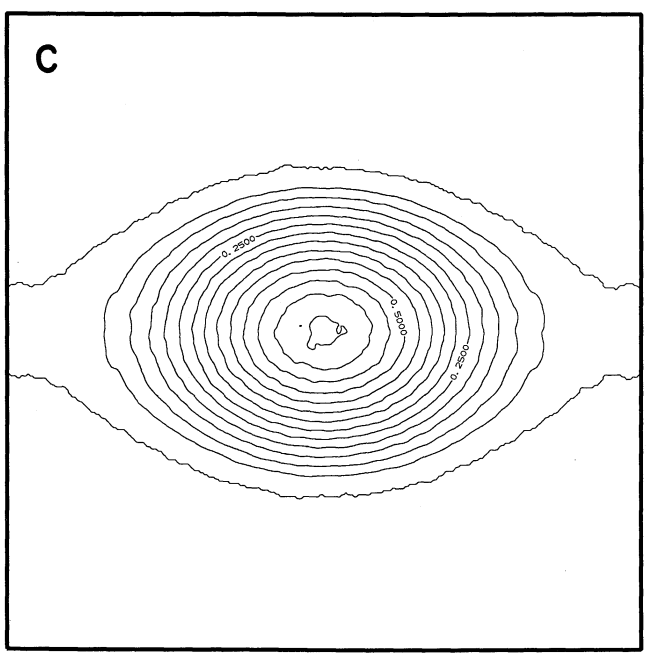

FIG. 2.—Density contours in the orbital plane at $t = 15$ for different models near the critical point of the $\Gamma = 2$ compressible Roche sequence: (*a*) $\mu = 0.060$; (*b*) $\mu = 0.070$; (*c*) $\mu = 0.075$. The scale is linear, with the nth contour corresponding to $\rho_n = n \times (0.05MR^{-3})$. The outermost contour corresponds to $\rho = 0$. The region covered is $-2 < x$, $y < 2$, in units of R. Some mass shedding near the axis is clearly apparent in (*b*) and (*c*).

solution obtained by a linear perturbation technique. However, to zeroth order, if we assume that the physical conditions in the interior have changed very little, it is clear that $\Phi_0 = -GM/R$, as in the unperturbed polytrope. With this approximation, the solution near the surface is completely determined by equation (38).

We can rewrite the solution in a more useful, dimensionless form by using the following relation for a spherical polytrope of index $n = 1/(\Gamma - 1)$,

$$A = \frac{4\pi G}{(n+1)} \left(\frac{R}{\xi_1}\right)^2 \rho_c^{1-1/n} , \tag{39}$$

where the central density

$$\rho_c = \frac{\xi_1^3}{|\xi^2\theta'|_{\xi_1}} \left(\frac{M}{4\pi R^3}\right) . \tag{40}$$

Here ξ and θ are the usual Lane-Emden variables (see e.g., Chandrasekhar 1939), and ξ_1 is the first zero of $\theta(\xi)$. Equations (38)–(40) with $\Phi_0 = -GM/R$ give

$$\frac{\rho}{\rho_c} = \left[\frac{|\xi^2\theta'|_{\xi_1}}{\xi_1}\left(\frac{|\Phi|}{GM/R} - 1\right)\right]^{1/(\Gamma-1)} . \tag{41}$$

This ratio is plotted in Figure 3 (*dashed line*) for $\Gamma = 5/3$ and remains very close to the SPH solution in the region near the surface where $\rho/\rho_c \lesssim 0.1$.

The value $a_{\rm crit}$ of the binary separation corresponding to the critical (i.e., terminal) equilibrium solution is determined from the conditions

$$\Phi_0 = \Phi(x = x_{\rm crit}, y = 0, z = 0) , \tag{42}$$

where $x_{\rm crit}$ is such that

$$\left(\frac{\partial\Phi}{\partial x}\right)_{x=x_{\rm crit}, y=z=0} = 0 . \tag{43}$$

When these conditions are satisfied, the surface of the primary passes through the saddle point of the potential along the axis (the Langrange point L_1). Equations (36), (42), and (43) with $\Phi_0 = -GM/R$ give

$$\frac{a_{\rm crit}}{R} = \frac{3}{2}\left(\frac{3+q}{q}\right)^{1/3} ; \quad x_{\rm crit}/R = \frac{3}{2} . \tag{44}$$

Note that $x_{\rm crit}$ is independent of the mass ratio in the highly compressible limit. These results are included in Table 1 under $\Gamma = 1.2$ (corresponding to the "infinitely compressible" $n = 5$

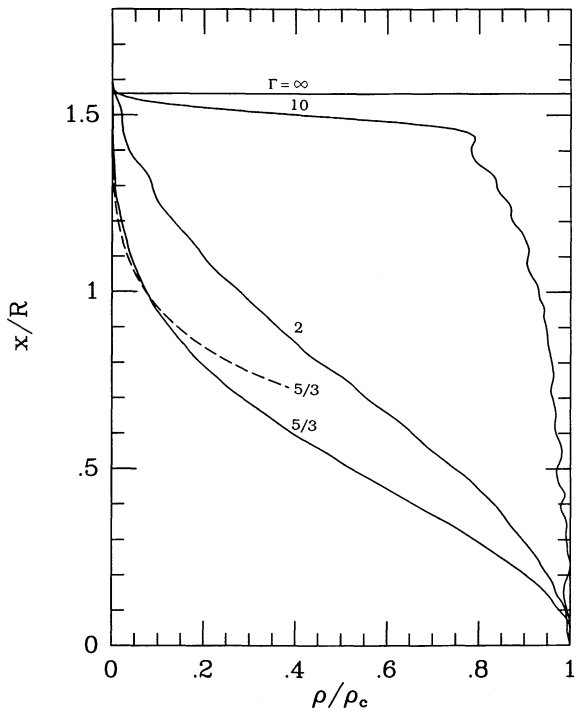

FIG. 3.—Interior density profiles of the critical configurations for various values of the adiabatic exponent Γ. The semimajor axis of each density contour in the orbital plane is plotted as a function of the ratio ρ/ρ_c for that contour. The horizontal line at the top, corresponding to the incompressible case, is from Chandrasekhar (1969). The profiles for Γ = 5/3, 2, and 10 are from our SPH calculations. The dashed line is the profile calculated from equation (41) for Γ = 5/3. Central densities in units of MR^{-3} are 0.24, 0.26, 0.79, and 1.4 for Γ = ∞, 10, 2, and 5/3.

polytrope, for which $\rho_c/\bar{\rho} = \infty$). It interesting to note that the ratio x_{crit}/R is not only independent of the mass ratio in the highly compressible limit, but depends also very little on the compressibility for any mass ratio, varying only from $x_{crit}/R = 1.5$ for Γ = 1.2 to $1.4 < x_{crit}/R < 1.6$ for $0 < q < 20$ in the incompressible limit (see Chandrasekhar 1969, chap. 8, Table XVIII).

In Table 1, we see that, already for Γ = 5/3, the parameters of the critical solution calculated by SPH agree well with our approximate analytical solution. In particular, the value $\mu_{crit} = 0.074$ determined numerically agrees very well with the analytical result $\mu_{crit} = 1/a^3_{crit} = 2/27 = 0.0741$ obtained from equation (44).

3.4. *The Darwin Problem*

More realistic models for synchronized binary stars can be constructed in SPH using a relaxation technique similar to the one described above for the Roche problem. At $t = 0$ we place two polytropes separated by a distance a along the x-axis. The construction of each polytrope takes place as before, using a uniform spatial distribution of particles on a cubic lattice and varying the particle masses to represent the density. The system is then allowed to relax in the presence of the combined gravitational field of both stars and the centrifugal potential. Here, in contrast to what was done for the Roche problem, *both the self-gravity and the tidal interaction* are calculated without approximations, by solving Poisson's equation on a grid overlapping both components.

The effects of rotation, however, are still represented by a centrifugal term in the SPH equations of motion:

$$\frac{dv_i}{dt} = F_i^{(\mathrm{Hydro})} + F_i^{(\mathrm{Grav})} + F_i^{(\mathrm{Rot})} - \frac{v_i}{t_{\mathrm{relax}}}, \qquad (45)$$

where $F_i^{(\mathrm{Rot})} = \Omega^2(x_i\hat{x} + y_i\hat{y})$. Care must be taken to calculate the centrifugal term in a way which remains consistent at all times with the distribution of mass in the system. The procedure we use is as follows. At $t = 0$, we calculate the total angular momentum of the system as $L_z = Q_{zz}\Omega$, where $Q_{zz} = \Sigma_i m_i(x_i^2 + y_i^2)$ and $\Omega = [G(M + M')/a^3]^{1/2}$. During the relaxation, L_z is then assumed to remain constant but Q_{zz} is constantly updated and the rotation frequency recalculated as $\Omega = L_z/Q_{zz}$. This procedure guarantees that the relaxation process remains physically reasonable, and that the final equilibrium structure is in a state of rigid rotation.

Figure 4 illustrates the results of such a relaxation calculation, performed here for two polytropes of equal masses with Γ = 2 and an initial binary separation $a = 2.9$ (units are such that $G = M = M' = R = 1$). By the end of the calculation, at $t = 15$, the separation has stabilized at the value $a = 2.83$. Contours of constant density in the orbital (x-y) plane and in the transverse (x-z) plane are shown. The equilibrium solution depicted in Figure 4 will be used as the starting point of our coalescence calculation in § 5. Indeed, this solution is actually unstable: if set into rotation and allowed to evolve *dynamically*, the two stars will merge completely in about one rotation period.

The same procedure can be used to calculate a sequence of models with decreasing binary separation, as we did for the Roche problem. Here, however, such a sequence does not terminate. It can be extended all the way to the point where the two stars are in contact (we refer to the corresponding solution as the *critical solution*). In fact, using SPH, it is even possible to construct equilibrium models where the two stars overlap. This is of little interest, however, since these models are dynamically unstable (cf. § 5). We have constructed numerically the sequence corresponding to $q = 1$ and Γ = 2. The deformation x_{crit}/R (where, as before, x is along the axis of the binary, increasing toward the point of contact between the two stars) of the critical solution along this sequence is given in Table 2. It is in excellent agreement with the results of semi-analytic perturbation calculations by Martin (1970) for polytropes of index $2 \leq n < 5$. For these very compressible polytropes, the parameters of the critical solution are nearly independent of the polytropic index (Martin 1970 finds that the deformation x_{crit}/R varies only between 1.365 and 1.375 for $2 \leq n \leq 4.9$). Table 2 also gives the result for the incompressible case, Γ = ∞, taken from Chandrasekhar (1969, chap. 8, Table XVIII). Note that this latter result was obtained in the context of the classical Darwin problem, where the tidal potential is truncated to quadratic terms.

Finally, to test our ability to calculate gravitational radiation waveforms, we took one of our equilibrium models with

TABLE 2

PROPERTIES OF THE CRITICAL SOLUTIONS FOR BINARY POLYTROPES

Γ	x_{max}/R	Source
1.2 to 1.5	1.37	Martin 1970
2	1.40	SPH
∞	1.42	Chandrasekhar 1987

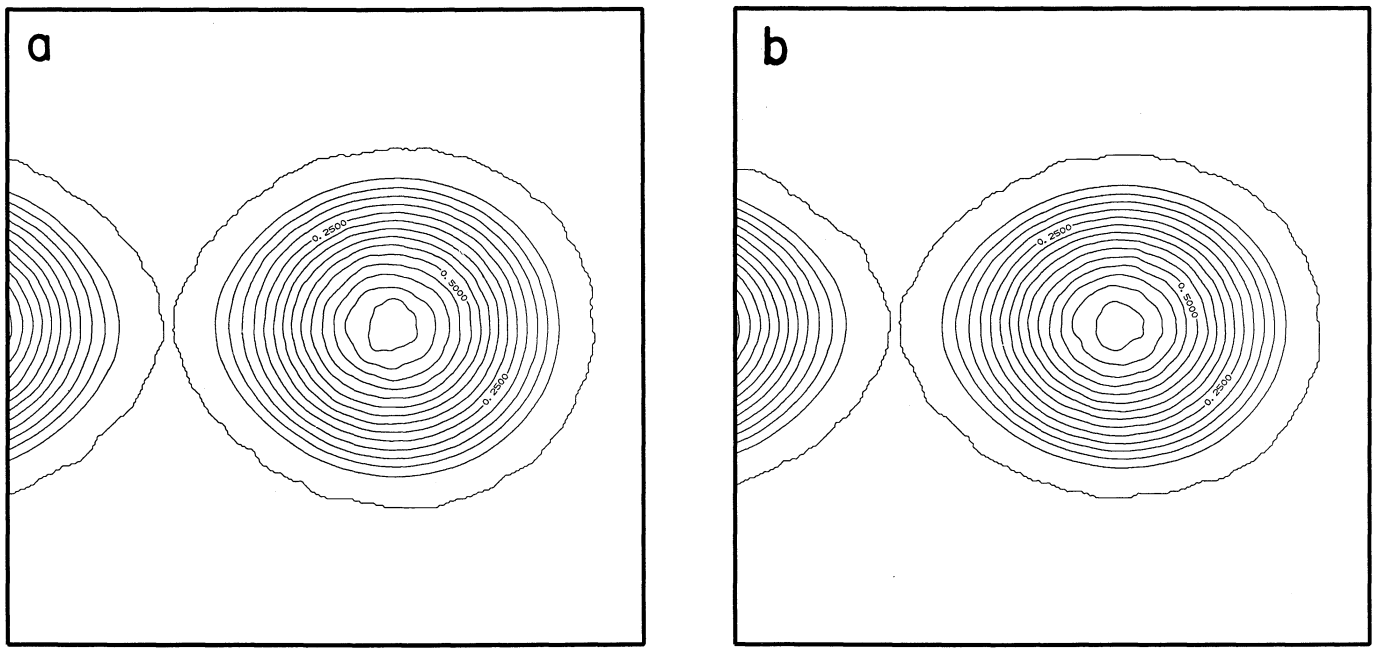

FIG. 4.—Density contours of an equilibrium binary star system. The contours were calculated as in Fig. 2. The binary contains two polytropes of equal masses with $\Gamma = 2$ and with a binary separation $a = 2.8$ (units are such that $G = M = M' = R = 1$). Cuts through the orbital plane (*a*) and the plane containing the rotation axis and the axis of the binary (*b*) are shown. The regions covered are $-1 < x < 3$ and $-2 < y, z < 2$. This configuration was used as the initial condition for our calculation of binary coalescence.

a rather large binary separation and we calculated its dynamical evolution. The equilibrium configuration determined in the corotating frame of the binary was set into motion and its dynamical evolution was calculated in the inertial frame (see § 5 for a discussion of stability). The corresponding gravitational radiation waveforms, calculated according to the method of § 2.2, for an observer situated along the rotation axis, are shown in Figure 5. Also shown are the theoretical waveforms calculated for two point masses on the same orbit. Clearly, the agreement is excellent. These results provide reassurance that our computed waveforms will be reliable and not the result of spurious fluid motions.

4. HEAD-ON COLLISIONS OF POLYTROPES

Head-on, axisymmetric collisions between identical polytropes provide an ideal test problem for this work. Indeed, they incorporate most of the ingredients of a coalescence calculation: strong, nonlinear hydrodynamical and gravitational interactions between the two stars, with shocks providing the dissipation. Because of its axisymmetry, the problem has already been well studied with more conventional finite-difference methods, which allow one to determine the solution with high spatial resolution. These calculations provide models for colliding neutron stars. Head-on collisions of two identical $\Gamma = 2$ polytropes have been calculated by Gilden & Shapiro (1984) (who also studied $\Gamma = 5/3$) and Evans (1987) in the Newtonian case, and are now being studied in full general relativity by Abrahams & Evans (1992). Some preliminary Newtonian calculations of off-axis collisions between neutron stars, using SPH, were also reported by Kochanek & Evans (1989).

The initial condition for our calculation is constructed as follows. We place two identical, unperturbed $\Gamma = 2$ polytropes along the x-axis, separated by a distance $4R$, where R is the stellar radius. This separation is large enough that we can

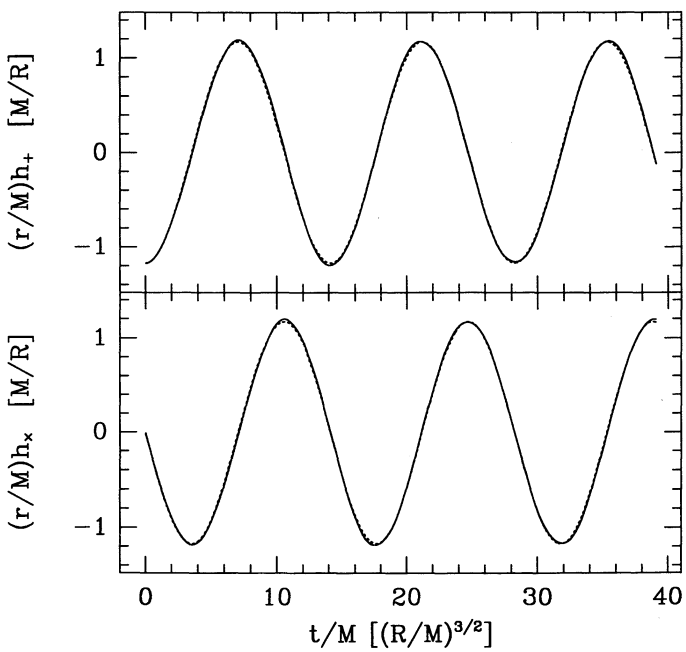

FIG. 5.—Gravitational wave emission from a stable binary system. The binary contains two $\Gamma = 2$ polytropes of equal mass M with a binary separation $a = 3.5R$. Geometrized units ($G = c = 1$) are used for measuring the parameters. Amplitudes of the two polarization states of the radiation are shown, as a function of retarded time t, for an observer along the rotation axis ($\theta = 0$) a distance r from the source. The solid lines are from our numerical calculation. The dashed lines (barely distinguishable) show the theoretical waveforms corresponding to two point masses with the same binary separation.

neglect tidal deformations at $t = 0$. All fluid particles in each star are given the same initial velocity, corresponding to a head-on, parabolic trajectory of their centers of mass. Each polytrope is constructed as in § 3, using $N = 8000$ particles per star. The results we quote in this section are in units such that $G = M = R = 1$, where M and R are the mass and radius of one polytrope. Our calculation extends to $t_f = 20$ in these units. Conservation of total energy is maintained to better than 1% throughout the calculation (cf. Fig. 6).

The evolution of the system can be summarized as follows (see also Gilden & Shapiro 1984). As the two stars come into contact, two recoil shocks form and begin to propagate into each star along the collision axis. The shock-heated gas in the central region immediately accelerates in the transverse direction, where it is not being contained by ram pressure. We find that about 5% of the total mass eventually escapes from the system. The rest, after it reaches a maximum expansion, recontracts supersonically, leading to a second phase of shock-dissipation in the system. After a few more large amplitude, nonadiabatic oscillations, the system stabilizes into a hot, pulsating, nearly spherical equilibrium configuration. The initial shock-heating, as well as the ensuing nonadiabatic pulsations can be seen most clearly in Figures 6 and 7, where we show the time evolution of total internal energy and total entropy in the system. For $2 \lesssim t \lesssim 3$, the two recoil shocks propagate through the stars, leading to a steep rise in entropy and internal energy. For $3 \lesssim t \lesssim 6$, the gas is expanding adiabatically, implying a decrease in internal energy and a plateau in entropy. For $6 \lesssim t \lesssim 20$, the internal energy oscillates, while the total entropy increases monotonically, implying that different regions of the gas are not recollapsing in phase. Finally, for $t \gtrsim 20$, the pulsations become nearly adiabatic and the total entropy levels off. This evolution is qualitatively in good agreement with that found by Gilden & Shapiro (1984).

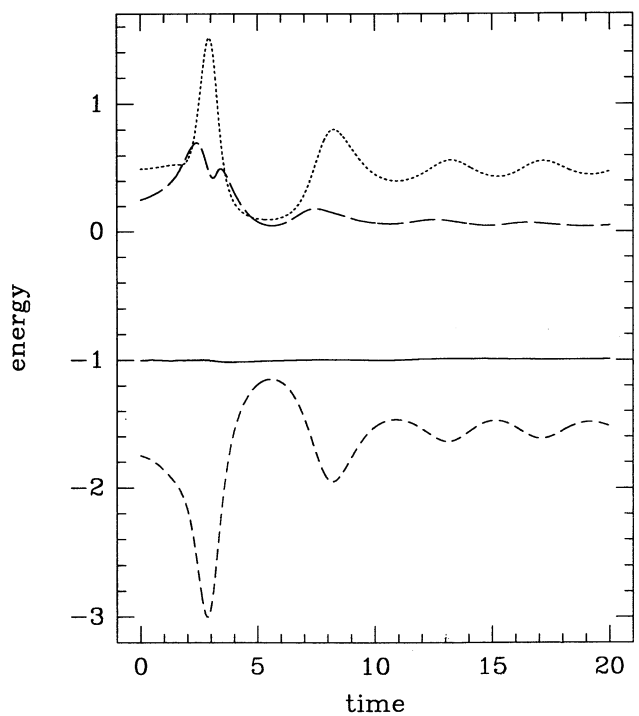

FIG. 6.—Time evolution of the various energies during the head-on collision of two polytropes with equal masses and $\Gamma = 2$. The potential energy (*short-dashed line*), internal energy (*dotted line*), kinetic energy (*long-dashed line*), and total energy (*solid line*) are shown

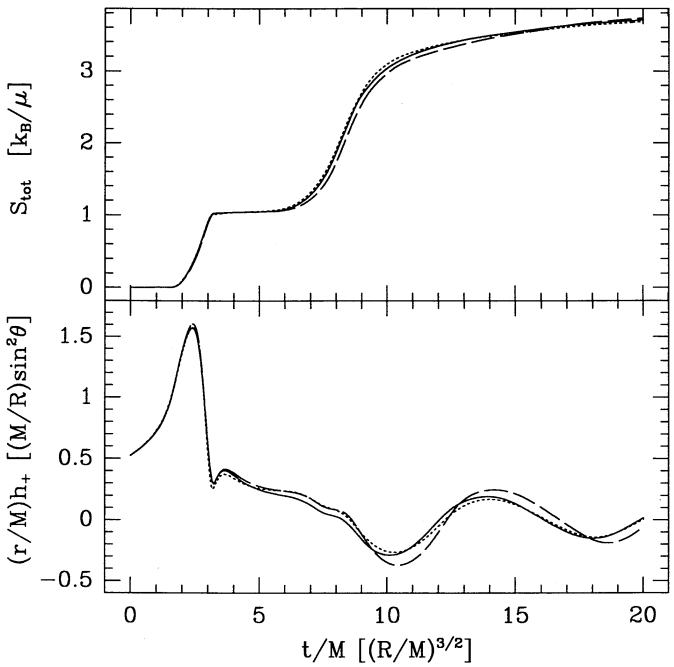

FIG. 7.—Time evolution of the total entropy and gravitational radiation waveform for the head-on collision of two $\Gamma = 2$ polytropes with equal mass M. The total entropy is calculated according to eq. (13), with the arbitrary constant S_0 calculated in such a way that $S_{tot} = 0$ at $t = 0$. The time and wave amplitude are measured in geometrized units. The three lines correspond to calculations with different parameters: the solid line is for $N = 8000$ particles per star and $N_N = 64$; the dotted line is for $N = 4000$ particles per star and $N_N = 32$; the dashed line is for $N = 16{,}000$ particles per star and $N_N = 64$.

Also shown in Figure 7 is the gravitational radiation waveform corresponding to the collision, calculated by the method of § 2.2. For an axisymmetric system, the only nonvanishing polarization is h_+, and is given by

$$h_+ = \frac{3}{2r}\frac{G}{c^4}\frac{d^2 I_{zz}}{dt^2}\sin^2\theta\,. \tag{46}$$

To check the sensitivity of our numerical results to changes in the integration parameters, we repeated the calculation with three different combinations of the number of particles N and the number of neighbors N_N (cf. § 3). Our "reference" calculation was performed with $N = 8000$ particles per star and $N_N \approx 64$; it took about 20 CPU hours on an IBM 3090-600J supercomputer. The corresponding results are shown by the solid line in Figure 7. To test the influence of *numerical noise*, we repeated the calculation with $N = 4000$ particles per star and $N_N \approx 32$ [this does not change $h \propto (N_N/N)^{1/3}$]. The results were practically unchanged (cf. Fig. 7, *dotted line*). To test the influence of *spatial resolution*, we performed a calculation with $N = 16{,}000$ particles per star and $N_N \approx 64$ (this makes h about 25% smaller). The results were again barely changed (cf. Fig. 7, *dashed line*), perhaps with the exception of a slightly higher amplitude in the gravitational radiation waveform. In Figure 8, we show a more detailed comparison of the three SPH results for the early development of the waveform, and we also compare our results to those of a recent finite-difference calculation (Abrahams & Evans 1992). For the main peak in the

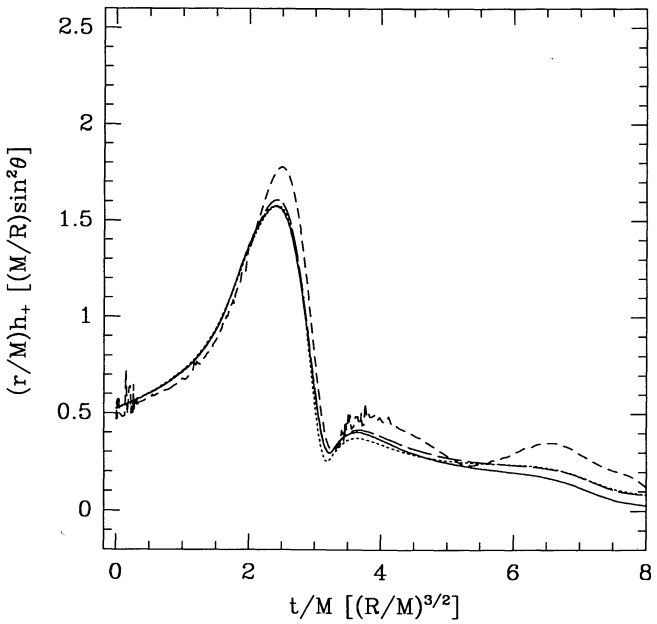

FIG. 8.—Comparison of waveforms at early times for the head-on collision. Conventions for the three SPH results are as in Fig. 7. In addition, the short-dashed line shows the result of a recent finite-difference calculation (Abrahams & Evans 1992).

wave amplitude, the difference between the two methods is $\lesssim 10\%$, and may be due to the higher spatial resolution of the finite-difference calculation.

The evolution of the total luminosity of gravitational radiation, calculated from equation (20), is shown in Figure 9. Most of the luminosity comes from the rapid *deceleration* of the matter during the propagation of the recoil shocks. This corresponds to the second peak in Figure 9. Instead, the much smaller first peak corresponds to the initial free-fall of the two stars. For comparison, the luminosity corresponding to the case of two point masses is also shown (*dashed line*). The total energy radiated in gravitational waves during the collision is $\Delta\epsilon_{GW} \approx 0.6/c^5$ in our units, or $\Delta\epsilon_{GW} \approx 0.6 \times 10^{52}\ M_{1.4}^{9/2}\ R_{10}^{-7/2}$ ergs, where $M_{1.4}$ is the mass of one star in units of 1.4 $M_\odot$ and R_{10} is the stellar radius in units of 10 km. This corresponds to an efficiency $\Delta\epsilon_{GW}/Mc^2 \approx 2.4 \times 10^{-3}\ M_{1.4}^{7/2}\ R_{10}^{-7/2}$, comparable to that found by Gilden & Shapiro (1984).

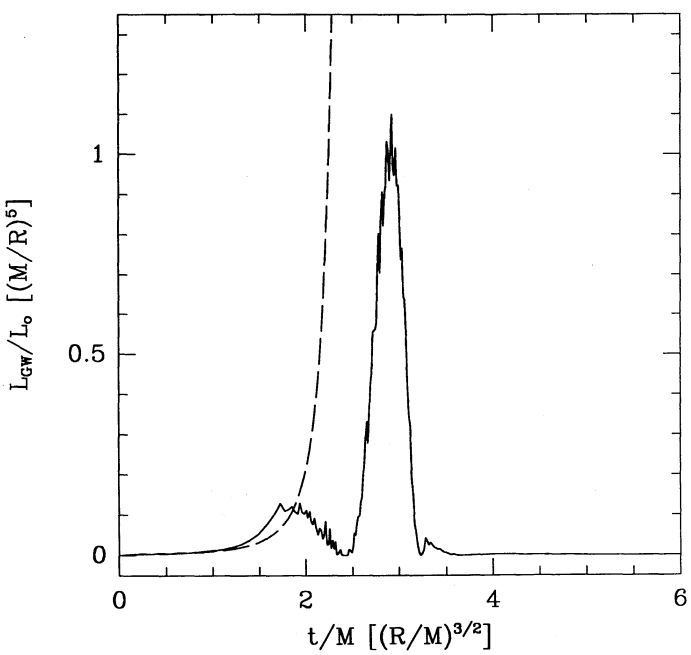

FIG. 9.—Gravitational radiation luminosity vs. retarded time for the head-on collision depicted in Figs. 6–8. Here $L_o \equiv c^5/G = 3.6 \times 10^{59}$ ergs s^{-1}. The solid line is our SPH result (for $N = 16{,}000$ particles per star and $N_N = 64$). The dashed line shows the theoretical result for two point masses.

5. COALESCENCE OF A BINARY POLYTROPE

Following the procedure described in § 3 we can construct, for a given mass ratio $q = M/M'$ and adiabatic index Γ, a sequence of equilibrium models with decreasing binary separation. As we have seen, the sequence can be followed all the way to the point where the surfaces of the two stars come into contact. However, we expect these equilibrium solutions to become *dynamically unstable* to tidal disruption somewhat *before* the point of contact. Indeed, analytical studies, based on the tensor virial method, have established this for the case of incompressible components with $q = 1$ (Chandrasekhar 1975; Tassoul 1975). A survey of equilibrium, $q = 1$ sequences with various adiabatic indices, which we performed using SPH, reveals that the same result is true in the compressible case: *for binaries containing two polytropes of equal masses, dynamical instability sets in just before the point of contact along an equilibrium sequence with decreasing binary separation.* The growth of the unstable mode leads to the coalescence of the two components on a time scale comparable to the orbital period. Using SPH, we can follow the full nonlinear evolution of the instability, and determine the final fate of the system. The starting point of our coalescence calculation is the equilibrium model shown in Figure 4. This model is just past the critical point for dynamical instability, which for the $\Gamma = 2$, $q = 1$ sequence, corresponds to a binary separation $a_{dyn}/R \approx 3$ (for comparison, in the incompressible case, $a_{dyn}/R = 2.90$; cf. Tassoul 1975). The onset of instability is illustrated in Figure 10, which shows the dynamical evolution of the binary separation for one model just before the critical point, and one model just past the critical point (the emission of gravitational radi-

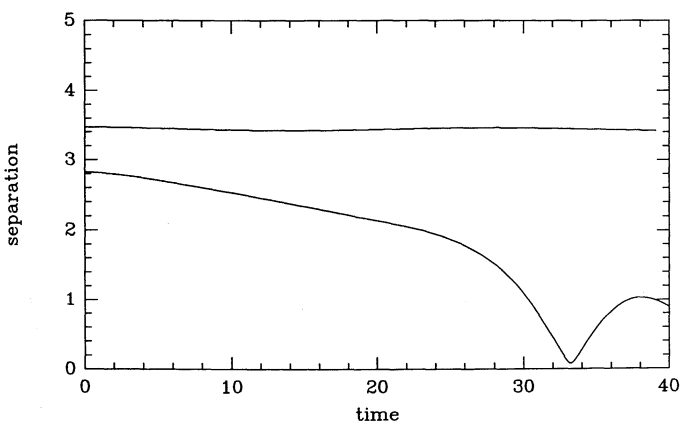

FIG. 10.—Time evolution of the binary separation for two equilibrium models. The model with initial separation $a/R = 3.5$ is stable. The other model, with initial separation $a/R = 2.8$ is unstable and leads to the coalescence of the two neutron stars on a time scale comparable to the initial orbital period ($P_{orb} \approx 21$ in units where $G = M = R = 1$).

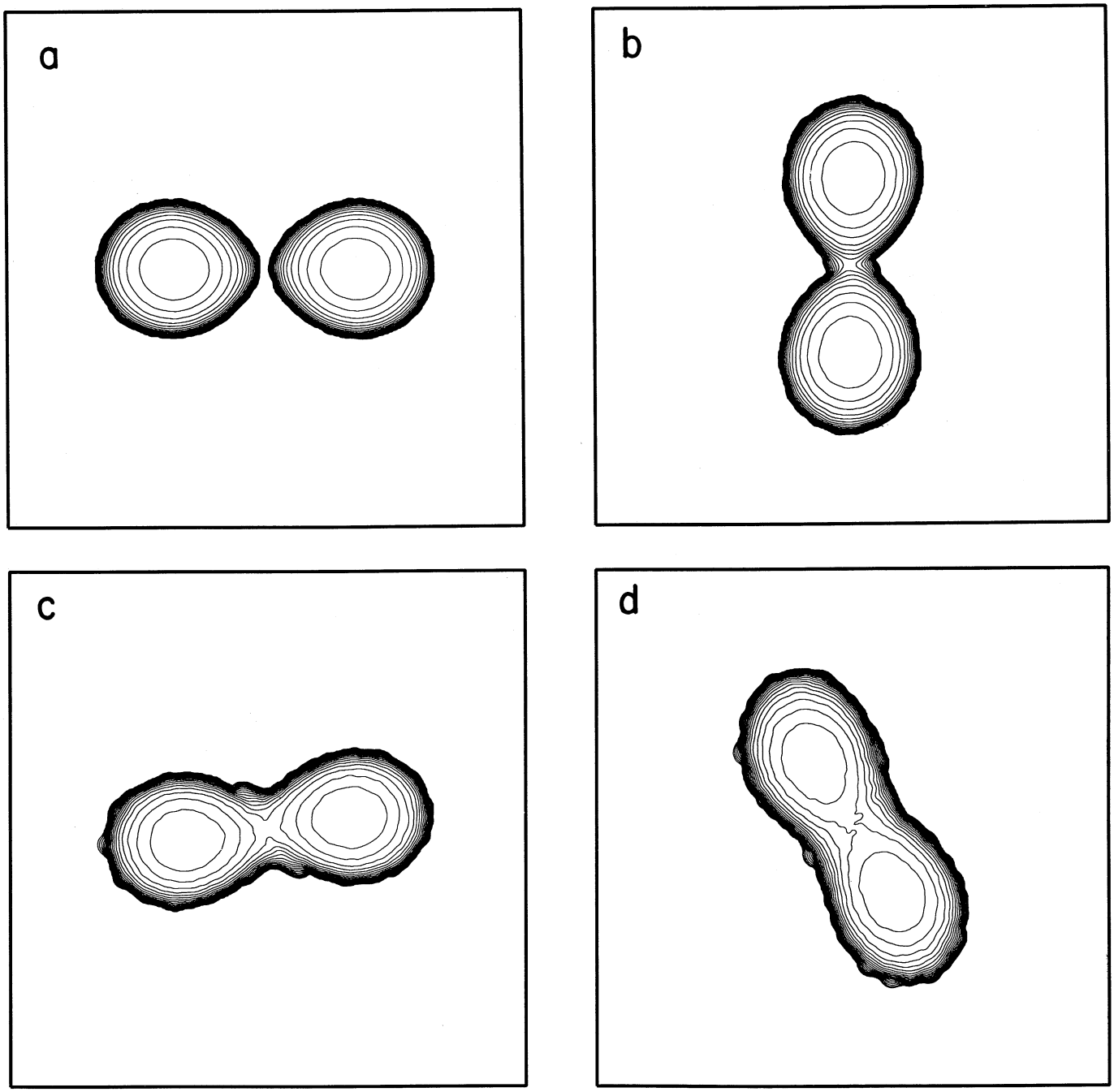

FIG. 11.—Coalescence of the binary depicted in Fig. 4. Contour plots of the density in the orbital plane are shown at various times. The region covered is $-4 < x, y < 4$. The scale is logarithmic with 16 contours covering 4 decades down from the maximum. (*a*) $t = 0$; (*b*) $t = 5$; (*c*) $t = 10$; (*d*) $t = 15$; (*e*) $t = 20$; (*f*) $t = 25$; (*g*) $t = 30$; (*h*) $t = 35$; (*i*) $t = 40$; (*j*) $t = 60$.

ation from the stable model was calculated in § 3 as a test of our method).

The development of the instability and the following hydrodynamical evolution of the system are shown in Figure 11. As before, we use units such that $G = M = R = 1$, where M and R are the mass and radius of one *unperturbed* star. Assuming that both stars have a mass $M \approx 1.4\ M_\odot$ and an unperturbed radius $R \approx 10$ km, the initial binary separation is $a \approx 28$ km and the initial orbital period $P_{\rm orb} \approx 1.5$ ms. The entire evolution shown in Figure 11 then takes about 5 ms. Contours of constant density in the orbital plane are plotted for various times. The density scale is logarithmic, covering 4 decades down from $\rho_{\rm max}$, with four contours per decade: the nth contour has $\rho_n/\rho_{\rm max} = 10^{-n/4}$. The rotation is counterclockwise. Consecutive plots are separated by about one-quarter of the initial orbital period. The entire calculation, performed with $N = 8000$ particles per star, $N_N \approx 64$, and a 256^3 grid for the gravitational field, took about 100 CPU hours on an IBM 3090-600J supercomputer.

We can distinguish three stages in the evolution of the system. In the initial development of the instability (Figs. 11*a*–11*d*), the surfaces come into contact and the two stars then

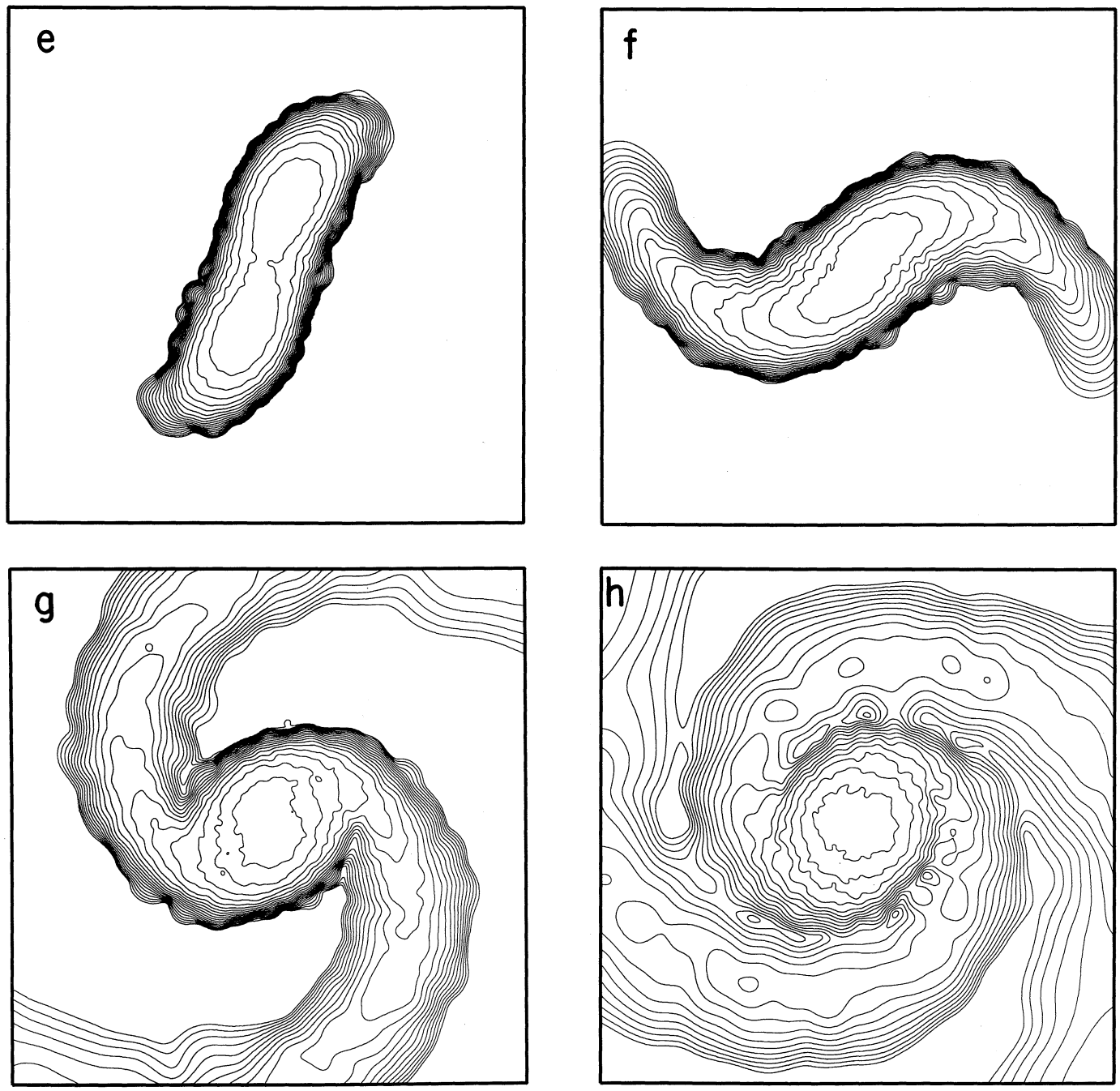

FIG. 11—*Continued*

begin merging. In the corotating frame of the binary, the radial infall velocities of the merging regions remain nearly constant in time, and very subsonic, so that the evolution is adiabatic at this stage. After about one complete revolution, when the inner regions of the two stars begin their radial infall, mass shedding sets in rather abruptly: matter near the periphery of the system starts spiraling outwards (Figs. 11*e*–11*g*). The evolution is still adiabatic. In the final stage, the spiral arms widen and merge together (Figs. 11*h*–11*j*). The relative radial velocities of neighboring arms are now supersonic, leading to shock-heating and dissipation. As a result, a hot, nearly axisymmetric rotating halo forms around the central dense core. Most of the gas in the halo remains bound to the core, with the total amount of mass loss being less than 0.1% at the end of the calculation. Throughout its evolution, the system remains very close to virial equilibrium. This is in contrast to the case of a head-on collision, where a large initial excess of kinetic energy has to be converted into other forms (mostly gravitational potential energy as can be seen in Fig. 6).

We can better understand these results by following the evolution of the ratio $T/|W|$ of the kinetic energy of rotation to the gravitational binding energy (Fig. 12). We know (cf.

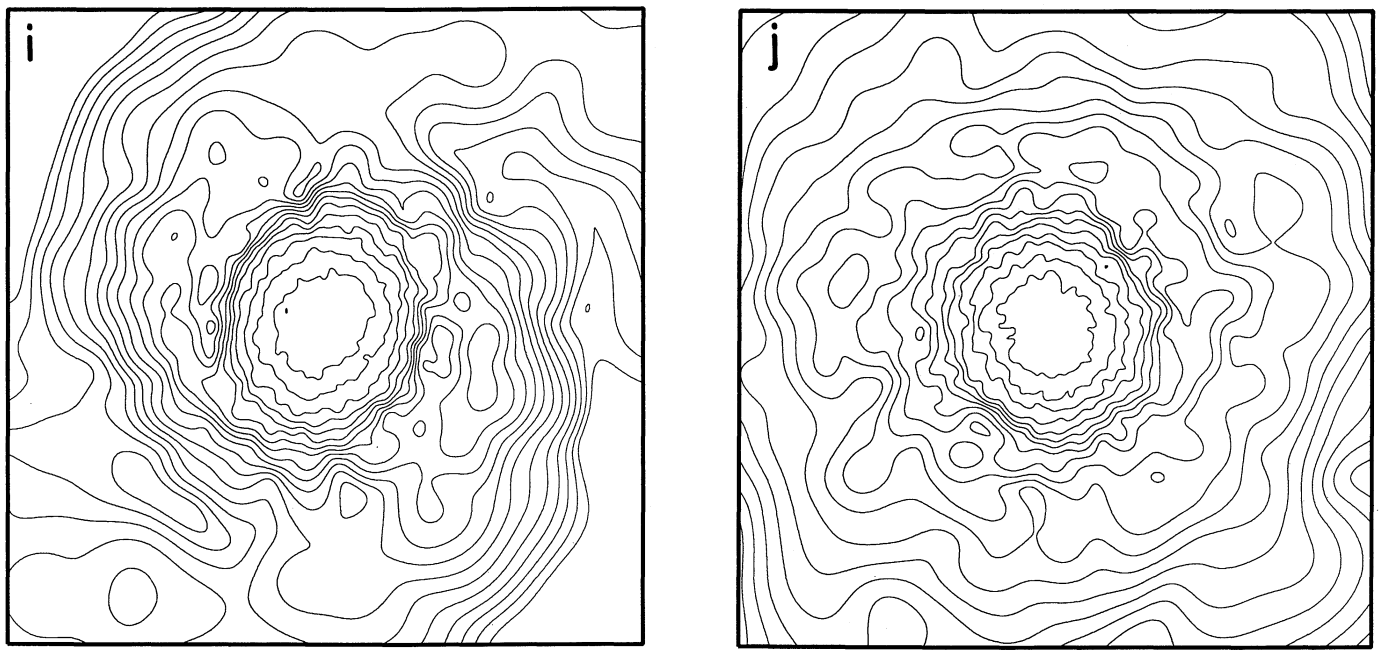

FIG. 11—*Continued*

James 1964) that a uniformly rotating polytrope with adiabatic index $\Gamma < 2.25$ (polytropic index $n > 0.8$) cannot form a barlike structure (the equivalent of an incompressible Jacobi ellipsoid). This is because the corresponding value of $T/|W|$ for the bar-mode instability would be larger than the critical value $(T/|W|)_{\max}$ beyond which mass shedding occurs. For $\Gamma = 2$ this terminal point along the equilibrium sequence corresponds to $(T/|W|)_{\max} = 0.12$ (see, e.g., Tassoul 1978). As the initial coalescence takes place, $T/|W|$ increases well above 0.12, making it necessary for some mass shedding to occur. The mass shedding continues until an axisymmetric configuration is reached. If rigid rotation were maintained throughout the mass shedding phase, the ratio $T/|W|$ would then decrease until it reaches 0.12. Instead, we find that a slightly larger value, $T/|W| \approx 0.14$, is reached, indicating that some amount of *differential rotation* must be present in the final configuration (see below).

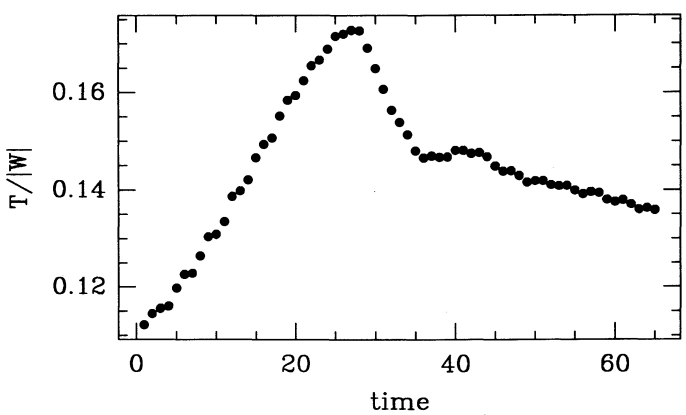

FIG. 12.—Time evolution of the ratio of rotational kinetic energy T to gravitational binding energy $|W|$ for the coalescence depicted in Fig. 11.

The structure of the final equilibrium configuration is shown in Figures 13–16. It consists of a rapidly rotating, uniform density core embedded in an extended, low-density halo. The core contains most of the mass: about 70% of the total mass is contained within a region of radius $r_c \approx 1$, where $\rho/\rho_c > 0.1$ (cf. Fig. 14). In our units the central density is $\rho_c \approx 0.8$, giving $\rho_c \approx 2 \times 10^{15}$ g cm^{-3} $M_{1.4} R_{10}^{-3}$, where $M_{1.4}$ is the mass of the neutron star in units of 1.4 $M_\odot$ and R_{10} is its radius in units of 10 km. This is very close to the central density of our unperturbed polytropic model. Some spiral structure is still apparent in the outer regions of the halo, where the density $\rho/\rho_c < 10^{-5}$ (cf. Fig. 13).

The rotation in the core is nearly uniform, with an angular velocity $\Omega_c \approx 0.6$ in our units, corresponding to a rotation period $(2\pi/\Omega)_c \approx 0.8$ ms $M_{1.4}^{-1/2} R_{10}^{3/2}$. The dispersion observed for $r < 1$ in Figure 15 is a numerical artifact: the ratio v/r becomes ill-defined as $r \to 0$. Differential rotation is evident in the halo, with the angular velocity following very closely a power-law of the type $\Omega \propto r_{\rm cyl}^{\nu}$, where $r_{\rm cyl} = (x^2 + y^2)^{1/2}$ is the distance to the rotation axis and $\nu \approx -1.8$. Note that, since the specific entropy is not constant in the halo (cf. Fig. 15), Ω need not be a function of $r_{\rm cyl}$ only. The fact that it is, to a very good approximation, implies that the halo has the structure of a *pseudo-barotrope* (see e.g., Tassoul 1978, chap. 4): the surfaces of constant density nearly coincide with those of constant pressure, even though the equation of state is *not* of the form $P = f(\rho)$. The exponent of the power-law is consistent with the stability condition for pseudo-barotropes, the so-called Solberg criterion, that the specific angular momentum $j = \Omega r_{\rm cyl}^2$ must increase outward (cf. Tassoul 1978, chap. 7). Stability also requires the specific entropy to increase outward. This condition is satisfied throughout most of the halo (cf. Fig. 15), except in the outermost region where the final equilibrium has probably not yet been reached [the hydrodynamical time scale in that region is very long: $(G\rho)^{-1/2} \gtrsim 100$].

We can roughly estimate the temperature of the gas in the halo by equating the kinetic pressure $\rho k_B T/\mu$, where μ is the

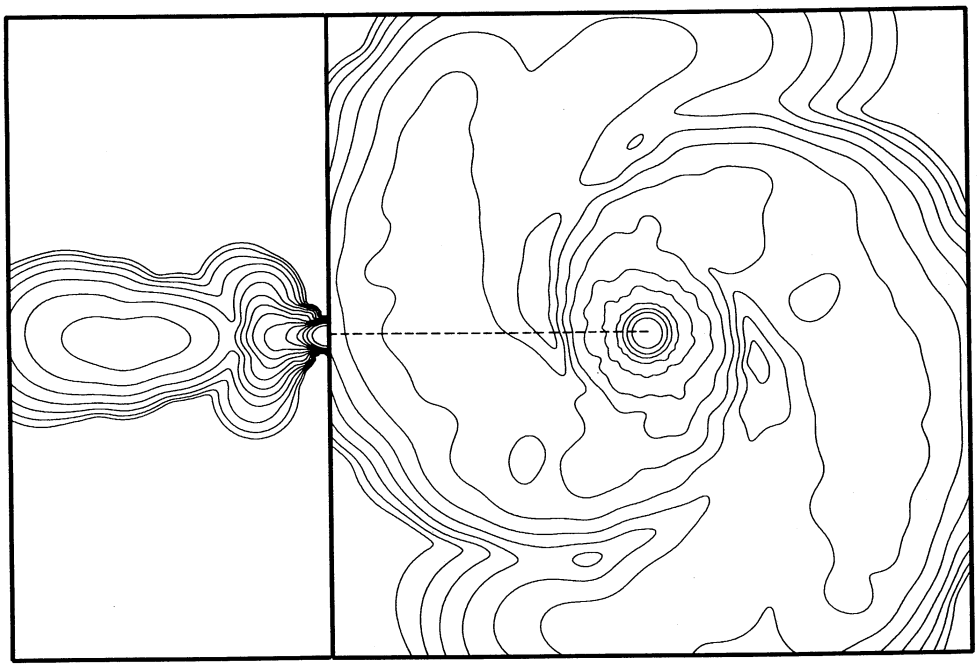

FIG. 13.—Density contours of the final configuration for the coalescence depicted in Fig. 11. The right panel shows a cut through the orbital plane. The left panel shows a cut through a plane containing the rotation axis (and intersecting the orbital plane along the dashed line). The region shown is $-20 < x, y, z < 20$. The scale is logarithmic, with 16 contours covering 8 decades down from the maximum.

mean molecular weight and k_B is Boltzmann's constant, to the difference $P - A_0\rho^\Gamma$, where $P = A\rho^\Gamma$ is the total pressure and A_0 is the constant, "cold" (i.e., pre-shock) value of A at $t = 0$. The maximum temperature in the halo is then $k_B T_{max}/\mu \approx 0.06$ in our units, giving $T_{max} \approx 1.3 \times 10^{11}$ K $M_{1.4}\, R_{10}^{-1}$ for μ equal to a baryon rest mass (this is comparable to the temperature in the interior of a nascent neutron star formed in a supernova explosion). This high-temperature region corresponds to the bulge at $r \approx 5$ in Figure 13. The average density in this region

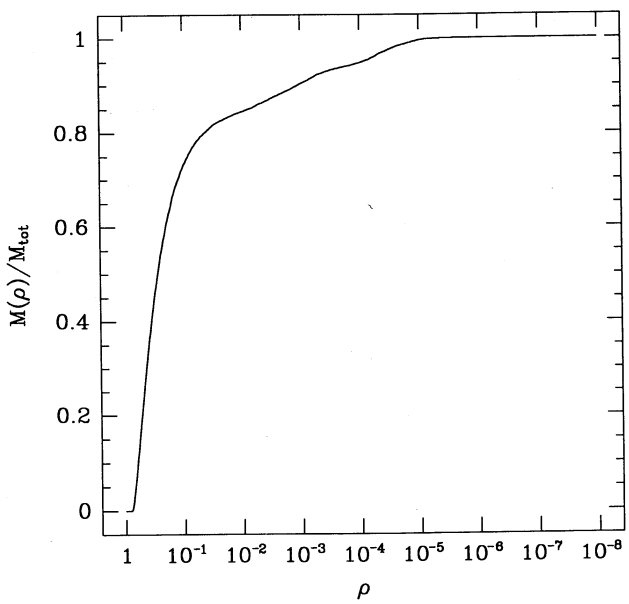

FIG. 14.—Mass profile of the final coalesced configuration for the merger depicted in Fig. 11. The mass fraction contained inside a constant density surface is plotted as a function of the value of the density on that surface.

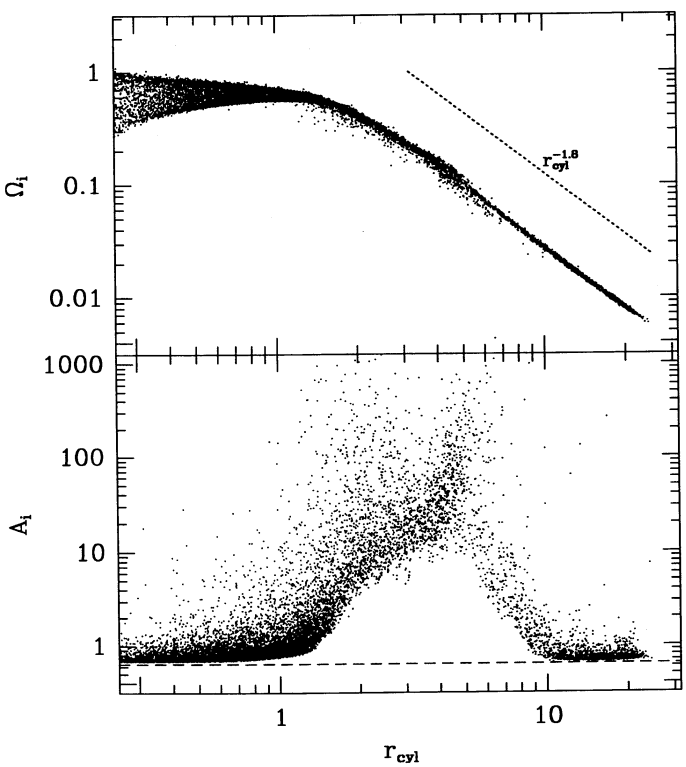

FIG. 15.—Profiles of the angular velocity of rotation Ω and entropy variable A in the final configuration for the merger depicted in Fig. 11. One dot is plotted for each SPH particle. The horizontal dashed line shows the value of A in the initial configuration. The cylindrical radius $r_{cyl} = (x^2 + y^2)$ is measured from the rotation axis.

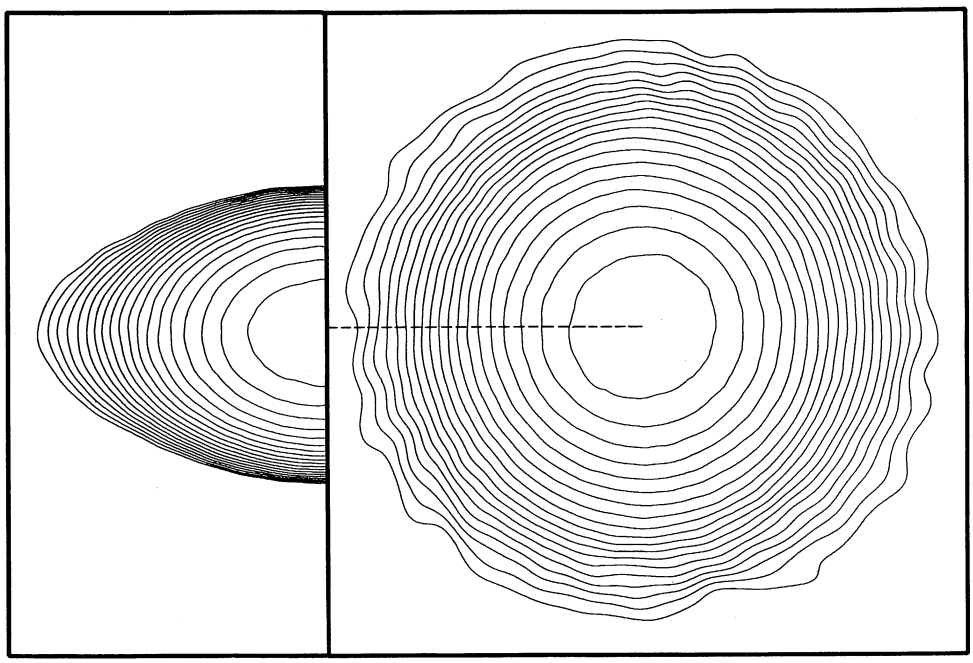

FIG. 16.—Density contours in the core of the final configuration for the merger depicted in Fig. 11. The right panel shows a cut through the orbital plane. The left panel shows a cut through a plane containing the rotation axis (and intersecting the orbital plane along the dashed line). The region shown is $-2 < x, y, z < 2$. The scale is logarithmic, with 10 contours per decade.

is $\rho \sim 10^{-4}\rho_c \sim 10^{11}$ g cm^{-3}. Most of the heating is caused by shocks forming when the low-density inner edges of the expanding spiral arms collide with the outer edge of the central core. The interior of the core itself remains essentially unheated. This should be contrasted to case of a head-on collision, where the entire mass of the system must pass through the initial recoil shocks.

We have used the formalism of § 2.2 to study the emission of gravitational radiation during the coalescence. Table 3 gives the time evolution of all nonzero components of $\ddot{I}_{lm}$. (Numerically, we find $\ddot{I}_{lz} \sim 10^{-4}$, which gives an estimate of the numerical error on the other, nonzero components.) This table allows one to calculate the waves emitted in any direction (θ, ϕ) (cf. eq. [24] and [25]). As an illustration, Figure 17 shows the waveforms received at a distance r from the source by a distant observer located on the rotation axis ($\theta = 0$). The two polarizations in this case are

$$rh_+ = \frac{G}{c^4}(\ddot{I}_{xx} - \ddot{I}_{yy}),$$

$$rh_\times = 2\frac{G}{c^4}\ddot{I}_{xy}. \qquad (47)$$

The maximum amplitude corresponds to $rh_{\max} \approx 2.4/c^4$ in our units, or $h_{\max} \approx 3 \times 10^{-21}\, M_{1.4}^2\, R_{10}^{-1} \times (r/10\ \mathrm{Mpc})^{-1}$. Note that, even though no dissipation mechanism was included in the calculation, the amplitude decays rapidly near the end of the evolution. This is simply because the distribution of mass in the system becomes more and more axisymmetric and steady as the new equilibrium is reached. The total luminosity of gravitational radiation is shown in Figure 18. There is a single, broad peak, with a maximum luminosity $L_{\max} \approx 0.8 \times 10^{56}$ ergs s^{-1} $M_{1.4}^5\, R_{10}^{-5}$, and with a width $\Delta t_{\mathrm{FWHM}} \approx 1.0$ ms $M_{1.4}^{-1/2}\, R_{10}^{3/2}$. The total energy radiated in gravitational waves during the final coalescence is $\Delta\epsilon_{\mathrm{GW}} \approx 8.8/c^5$ in our units, or $\Delta\epsilon_{\mathrm{GW}} \approx 10^{52}$ ergs $M_{1.4}^{9/2}\, R_{10}^{-7/2}$, corresponding to an efficiency $\Delta\epsilon_{\mathrm{GW}}/Mc^2 \approx 3.5 \times 10^{-2}\, M_{1.4}^{7/2}\, R_{10}^{-7/2}$. This is in excellent agreement with the most recent results of Oohara & Nakamura (1990), who quote efficiencies between 3% and 4.2% from similar calculations using a three-dimensional finite-difference

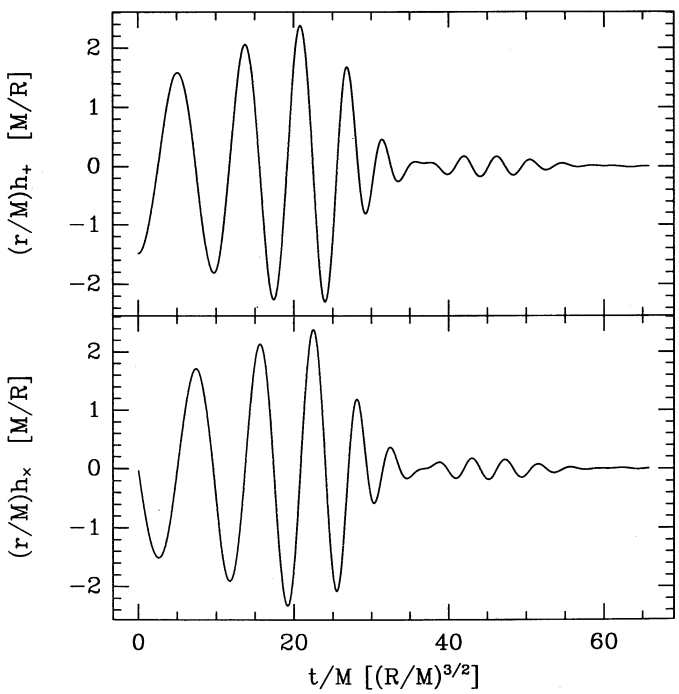

FIG. 17.—Gravitational radiation waveforms for the coalescence depicted in Fig. 11. Quantities are labeled in geometrized units. Amplitudes of the two polarization states of the radiation are shown for an observer situated along the rotation axis (at $\theta = 0$).

TABLE 3

GRAVITATIONAL RADIATION DATA

Time[a]	$\ddot{I}_{xx}$[b]	$\ddot{I}_{yy}$	$\ddot{I}_{zz}$	$\ddot{I}_{xy}$	Time[a]	$\ddot{I}_{xx}$[b]	$\ddot{I}_{yy}$	$\ddot{I}_{zz}$	$\ddot{I}_{xy}$
0.00000.....	−0.74145	0.74682	0.02420	−0.01876	32.75328.....	−0.00875	0.07999	0.03040	0.16381
0.56329.....	−0.68007	0.72014	0.03985	−0.25868	33.20978.....	−0.09224	0.13911	0.00860	0.09059
1.12065.....	−0.55974	0.58840	0.02559	−047783	33.68417.....	−0.11877	0.12908	−0.01574	0.00028
1.68303.....	−0.38321	0.37628	−0.00266	−0.64277	34.16769.....	−0.08782	0.07347	−0.02152	−0.06291
2.25932.....	−0.15297	0.11669	−0.02044	−0.73674	34.65138.....	−0.03154	0.01125	−0.00505	−0.08044
2.83430.....	0.11873	−0.14314	−0.00631	−0.74736	35.13223.....	0.02070	−0.02541	0.02212	−0.06212
3.39190.....	0.40483	−0.36545	0.03502	−0.66902	35.61092.....	0.04281	−0.03669	0.03638	−0.03212
3.93559.....	0.63526	−0.55732	0.05655	−0.50547	36.09766.....	0.03937	−0.03338	0.02995	−0.00984
4.48252.....	0.76739	−0.71213	0.03924	−0.27144	36.59766.....	0.02476	−0.03374	0.00595	−0.00061
5.03987.....	0.79011	−0.79413	−0.00377	0.00729	37.11234.....	0.01263	−0.04485	−0.01726	0.00314
5.61881.....	0.72283	−0.76184	−0.03045	0.30243	37.63681.....	0.00933	−0.05562	−0.02001	0.01483
6.19419.....	0.58704	−0.59356	−0.00797	0.56813	38.15901.....	0.01071	−0.04199	0.00237	0.03642
6.74890.....	0.38687	−0.31943	0.03997	0.76201	38.68169.....	−0.00124	0.00144	0.02959	0.05348
7.28868.....	0.10967	−0.00288	0.06434	0.85277	39.20020.....	−0.03100	0.05110	0.03756	0.04490
7.82589.....	−0.22535	0.29426	0.04145	0.82054	39.72968.....	−0.05674	0.07704	0.02010	0.00516
8.37457.....	−0.55372	0.54656	−0.00740	0.66387	40.27815.....	−0.05771	0.05397	−0.00968	−0.04736
8.95095.....	−0.79920	0.75663	−0.03082	0.39564	40.83446.....	−0.01819	−0.00601	−0.02292	−0.07783
9.52521.....	−0.89732	0.89564	−0.00126	0.05253	41.38687.....	0.04130	−0.06676	−0.00888	−0.06201
10.07730.....	−0.83351	0.90941	0.05072	−0.31142	41.93094.....	0.08764	−0.08326	0.02304	−0.00437
10.59555.....	−0.64952	0.75971	0.07059	−0.62666	42.47504.....	0.07748	−0.04943	0.03849	0.05984
11.12053.....	−0.37832	0.44630	0.04050	−0.85505	43.02368.....	0.01472	0.01662	0.02585	0.08738
11.65034.....	−0.04809	0.03818	−0.01251	−0.95022	43.58324.....	−0.06270	0.06912	−0.00567	0.05689
12.19145.....	0.32941	−0.37231	−0.03396	−0.89684	44.15462.....	−0.10005	0.07471	−0.02526	−0.01211
12.73807.....	0.70879	−0.71073	−0.00449	−0.68773	44.72858.....	−0.06692	0.03400	−0.01246	−0.07350
13.28469.....	0.97952	−0.93700	0.03080	−0.33395	45.28328.....	0.01102	−0.02467	0.01986	−0.08699
13.82915.....	1.05378	−1.00088	0.04134	0.10649	45.82436.....	0.07957	−0.06572	0.04121	−0.04708
14.38177.....	0.89707	−0.87254	0.02029	0.54778	46.36557.....	0.09055	−0.07215	0.03149	0.01858
14.95270.....	0.53247	−0.55232	−0.01368	0.89543	46.92780.....	0.03826	−0.03918	0.00006	0.06935
15.54012.....	0.03708	−0.07301	−0.02552	1.06161	47.49905.....	−0.03858	0.01329	−0.02298	0.07155
16.11436.....	−0.46520	0.45896	−0.00204	0.98683	48.06616.....	−0.08886	0.05113	−0.01815	0.02795
16.67711.....	−0.86949	0.91237	0.03188	0.66946	48.61411.....	−0.08014	0.05832	0.01214	−0.03008
17.23611.....	−1.09109	1.13964	0.03525	0.17024	49.14651.....	−0.02702	0.03277	0.03876	−0.06671
17.79855.....	−1.05284	1.07336	0.01063	−0.38762	49.67336.....	0.02839	−0.01198	0.03746	−0.06558
18.38383.....	−0.73634	0.72031	−0.01886	−0.87292	50.20724.....	0.05413	−0.05044	0.01105	−0.03199
18.98122.....	−0.18852	0.16579	−0.02037	−1.14116	50.76010.....	0.04074	−0.06169	−0.01846	0.01115
19.56808.....	0.45102	−0.43717	0.01065	−1.09118	51.33012.....	0.00389	−0.03794	−0.02317	0.03690
20.13969.....	0.97166	−0.92630	0.03486	−0.72006	51.88762.....	−0.02641	0.00099	0.00071	0.03252
20.72169.....	1.19920	−1.16852	0.02378	−0.11753	52.42769.....	−0.02984	0.03252	0.03077	0.00731
21.31165.....	1.05501	−1.06165	−0.00499	0.52570	52.96127.....	−0.01317	0.03679	0.04055	−0.01952
21.89012.....	0.61293	−0.63832	−0.01789	1.00361	53.50208.....	0.00407	0.01136	0.01924	−0.03177
22.44537.....	0.02426	−0.02598	−0.00053	1.19066	54.06067.....	0.01269	−0.02384	−0.01337	−0.02478
22.96873.....	−0.54501	0.58250	0.02435	1.05121	54.63173.....	0.00958	−0.04343	−0.02662	−0.00658
23.46965.....	−0.96200	1.01104	0.02816	0.64656	55.19231.....	0.00360	−0.03568	−0.00804	0.00950
23.95222.....	−1.13088	1.16329	0.01052	0.11091	55.73836.....	0.00286	−0.00982	0.02438	0.01382
24.43297.....	−1.03322	1.03780	−0.01165	−0.42411	56.27991.....	0.00599	0.01284	0.04211	0.00816
24.90866.....	−0.69703	0.69503	−0.01603	−0.83331	56.82246.....	0.00773	0.01729	0.02881	−0.00107
25.35677.....	−0.22671	0.25139	0.00153	−1.02517	57.36765.....	0.00228	0.00170	−0.00430	−0.00582
25.79015.....	0.27056	−0.19764	0.02695	−0.98361	57.92349.....	−0.00584	−0.01722	−0.02689	−0.00501
26.21445.....	0.66937	−0.55865	0.03843	−0.73278	58.48164.....	−0.00678	−0.02323	−0.01871	−0.00094
26.63626.....	0.87572	−0.75878	0.02565	−0.34667	59.03075.....	−0.00006	−0.01351	0.01360	0.00253
27.05774.....	0.86122	−0.75216	0.00163	0.06548	59.55533.....	0.00775	−0.00010	0.03809	0.00318
27.48387.....	0.65527	−0.55817	−0.01896	0.39996	60.07985.....	0.01408	0.00802	0.03844	0.00179
27.91629.....	0.33521	−0.23623	−0.02020	0.57727	60.61566.....	0.00903	0.00046	0.01046	0.00165
28.34753.....	0.00632	0.10856	−0.00110	0.56265	61.16989.....	−0.00184	−0.01169	−0.02016	0.00369
28.77936.....	−0.23477	0.37534	0.02473	0.38265	61.72348.....	−0.01330	−0.01986	−0.02836	0.00622
29.19954.....	−0.32860	0.47892	0.03653	0.12637	62.26967.....	−0.01210	−0.01181	−0.00409	0.00773
29.62546.....	−0.27757	0.41447	0.02906	−0.11626	62.80638.....	−0.00351	0.00520	0.02872	0.00658
30.06476.....	−0.12044	0.22689	0.00694	−0.26466	63.33981.....	0.00441	0.01776	0.04249	0.00223
30.51328.....	0.06517	0.00400	−0.01463	−0.27738	63.87347.....	0.00414	0.01543	0.02547	−0.00227
30.97162.....	0.20474	−0.16019	−0.02027	−0.17228	64.42429.....	−0.00345	−0.00092	−0.00849	−0.00435
31.41954.....	0.25311	−0.20616	−0.00338	−0.01950	64.98416.....	−0.01069	−0.01569	−0.02763	−0.00228
31.86652.....	0.20961	−0.14564	0.02117	0.11397	65.54245.....	−0.01050	−0.01693	−0.01483	0.00228
32.30769.....	0.10748	−0.03000	0.03570	0.17810					

[a] Time is in units of $(R^3/GM)^{1/2}$.

[b] $\ddot{I}_{lm}$ is in units of GM^2/R.

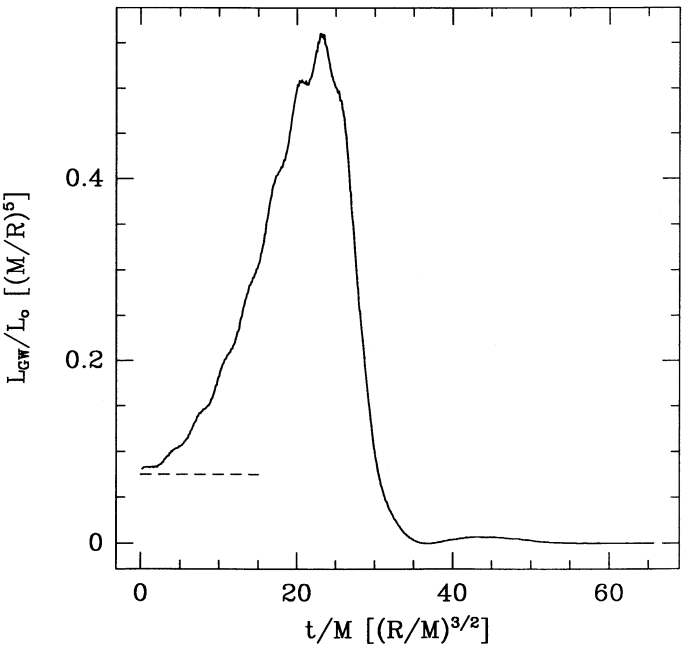

FIG. 18.—Gravitational radiation luminosity for the coalescence depicted in Fig. 11. The dashed line shows the theoretical estimate for two point masses in a (stable) binary with the same initial separation,

code which includes the gravitational radiation reaction. We have also compared our results to those of recent N-body simulations of the coalescence of two identical, *collisionless* clusters of point masses (Kochanek et al. 1990; see especially their Figure 11 for $r_0/R = 3$). We find surprisingly close agreement between the two calculations. This may be explained by the relatively small importance of shocks in this particular fluid calculation.

6. DISCUSSION

Our interpretation of the results of § 5 in terms of the ratio $T/|W|$ suggests that the final evolution of a coalescing neutron star binary may be strongly sensitive to the effective adiabatic index of the equation of state. Indeed, it is possible that for $\Gamma \gtrsim 2.25$, a *stable* nonaxisymmetric Jacobi-like ellipsoid could result from the initial merging of the two stars, with no mass shedding at all. Such an evolution would lead to a strikingly different signature in the gravitational radiation waveform. Indeed, the emission would remain that of a rotating bar, damped only by the radiation reaction. Moreover, preliminary calculations which we performed for polytropes with $\Gamma < 2$ indicate that the dynamical instability identified in § 5 disappears for sufficiently compressible configurations. In that case the initial merging itself will be driven by the radiation reaction rather than hydrodynamics. This motivates our forthcoming study (Rasio & Shapiro 1992) of the effects that a change in the adiabatic index will have on the solution.

In § 5 we found that, after mass shedding has occurred, the ratio $T/|W|$ stabilized at $\lesssim 0.14$. It is interesting to note that $T/|W| \approx 0.14$ is also the critical value for the onset of *secular instabilities* in many axisymmetric, differentially rotating structures (see, e.g., Tassoul 1978). Near the end of our calculation, a slow, steady decrease in $T/|W|$ (on a time scale ~ 100 times the inner rotation period) brings its value down to slightly below 0.14. However, this decrease may be caused by numerical dissipation effects. Therefore, there is the real possibility that a secular instability will, in fact, develop. If the gravitational radiation reaction is the only source of dissipation, this instability could lead to the formation of the compressible analog of a Dedekind ellipsoid (see e.g., Shapiro & Teukolsky 1983), i.e., a differentially rotating ellipsoid which maintains a stationary shape in the inertial frame. This configuration, just like our axisymmetric final configuration, does not generate gravitational radiation. Note, however, that the existence of the compressible analog of a Dedekind ellipsoid has never been demonstrated. In fact, it has been shown that the most straightforward generalization of the classical homogeneous Dedekind ellipsoid, i.e., a nonaxisymmetric inhomogeneous configuration stationary in the inertial frame and whose velocity has no meridional component and depends linearly on position, cannot exist (Ipser & Managan 1981).

When identical neutron stars of mass $\gtrsim 1\ M_\odot$ collide and merge, there is the possibility that gravitational collapse to a black hole will occur. It appears unlikely that rotation can prevent the collapse, even for the case of merging in a binary. Indeed, this would require a relativistic rotation parameter (see, e.g., Misner et al. 1970) $a/M_{\rm tot} > 1$. For a (Newtonian) binary with orbital separation r this parameter has the value

$$\frac{a}{M_{\rm tot}} = \frac{c}{G}\frac{J}{4M^2} \approx \frac{1}{8}\frac{c}{v_{\rm orb}} \approx 0.7\left(\frac{M}{1.4\ M_\odot}\right)^{-1/2}\left(\frac{r}{30\ \rm km}\right)^{-1/2}, \tag{48}$$

where J is the total angular momentum, M is the mass of one star, and $v_{\rm orb} = (GM/2r)^{1/2}$. Therefore we typically have $a/M_{\rm tot} < 1$ initially. In addition, gravitational radiation reaction can remove as much as 10% of the total angular momentum before the final configuration is reached (Oohara & Nakamura 1990). For all *parabolic* collisions equation (48) gives an upper limit for $a/M_{\rm tot}$ (the limit being reached for grazing incidence). Only in the case of a *hyperbolic* collision with near-grazing incidence could we have $a/M_{\rm tot} > 1$.

Thermal pressure support from shock-heated material is equally ineffective in halting the collapse during binary coalescence, since most of the mass evolves adiabatically (cf. § 5). One may wonder if different initial conditions would not lead to a more violent interaction between the two stars, with more material passing through shocks. Certainly, if the neutron-star spin rates Ω_s differed significantly from the orbital rotation rate $\Omega_{\rm orb}$, supersonic transverse motions could result if $|\Omega_s - \Omega_{\rm orb}|/\Omega_{\rm orb} \sim 1$. The qualitative evolution of the system in this case would likely be very different from that of a rigidly rotating binary. In future work (Rasio & Shapiro 1992), we will study the coalescence of such asynchronized binaries. We will also study the effectiveness of tidal interactions during the spiral-in phase of the evolution, and we will try to constrain the magnitude of the desynchronization just before the final merging.

Even in rigidly rotating binaries, gravitational-radiation reaction does accelerate the inward radial motion of the two stars just before they come into contact. The effective radial velocity is (see, e.g., Shapiro & Teukolsky 1983)

$$v_r = -\frac{64}{5}\frac{G^3}{c^5}\frac{M^3}{r^3}, \tag{49}$$

corresponding to a Mach number

$$\mathcal{M} = 4 \times 10^{-3}\left(\frac{c}{c_s}\right)\left(\frac{M}{1.4\ M_\odot}\right)^3\left(\frac{r}{30\ \rm km}\right)^{-3}. \tag{50}$$

Since $c_s \lesssim c$ in massive neutron stars, we do not expect strong shocks to develop because of the radiation reaction. Indeed, in the calculations of Oohara & Nakamura (1990), which include the inward radial velocity of equation (49), shocks were found to remain negligible. Note that this is in contradiction with a basic assumption underlying several models of extragalactic gamma-ray bursts based on coalescing neutron-star binaries (see, e.g., Paczyński 1990).

In the case of truly colliding stars, however, shocks dominate the final evolution of the system (cf. § 4). The merged configuration will exceed the cold mass limit if the progenitor masses exceed about 1 $M_\odot$. It is only after the hot, quasi-equilibrium merged object has cooled by neutrino emission that the thermal pressure support will disappear. In that case, the final collapse to a black hole may be delayed by as much as a few seconds, after which a final burst of gravitational radiation will be emitted if the configuration is sufficiently nonspherical due to rotation.

What are the prospects for detecting the gravitational radiation emitted during the final merging of two neutron stars? Since the waves emitted during the merging have nonperiodic time dependences and have a duration short compared to a typical observation time, we are dealing with a *burst source*. This particular type of burst is known as a *burst without memory*, i.e., one in which $\boldsymbol{h}^{\rm TT}$ returns to zero after the burst is over (Thorne 1987). This is because there is no change in the $1/r$, Coulomb-type gravitational field of the source. (In a fully relativistic calculation, however, the nonlinearities of the field equations will in general introduce a nonzero memory, $\Delta \boldsymbol{h}^{\rm TT} \neq 0$, corresponding to the change in total mass-energy of the system; see Christodoulou 1991 and Thorne 1992.)

The best strategy for detecting such a burst without memory with broad-band detectors (like those of LIGO) involves the construction of an *optimal filter* (Thorne 1987). This construction requires that the waveform $\boldsymbol{h}^{\rm TT}(t)$ be known. Therefore, burst sources of gravitational radiation are best characterized by their complete waveform $\boldsymbol{h}^{\rm TT}(t)$. However, the detectability of a burst source can be studied approximately in terms of a single characteristic amplitude h_c and a single characteristic frequency f_c. The characteristic amplitude h_c should be compared to the amplitude $h_{3/\rm yr}$ of a source with sufficiently large signal-to-noise ratio that, if it is seen three times per year by LIGO, we can be 90% confident that the detectors are not just seeing their own noise (Thorne 1987).

It is beyond the scope of this paper to perform a detailed calculation of the characteristic amplitude h_c. However, we can roughly estimate h_c in terms of the total energy radiated by a source at distance r_0 as (Thorne 1987)

$$h_c \approx 2.7 \times 10^{-20} \left(\frac{\Delta \epsilon_{\rm GW}}{1\ M_\odot}\right)^{1/2} \left(\frac{f_c}{1\ \rm kHz}\right)^{-1/2} \left(\frac{r_0}{10\ \rm Mpc}\right)^{-1} . \quad (51)$$

Using our numerical result for $\Delta \epsilon_{\rm GW}/M$ (cf. § 5) and approximating f_c by twice the Keplerian orbital frequency at the moment of first contact between the two stars we get from equation (51),

$$h_c \approx 0.9 \times 10^{-20} M_{1.4}^2 R_{10}^{-1} \left(\frac{r_0}{10\ \rm Mpc}\right)^{-1} . \quad (52)$$

For the LIGO project, once advanced detectors with light recycling are used, the sensitivity to bursts with $f_c \sim 10^3$ Hz (limited by photon shot noise) is expected to be (Thorne 1987)

$$h_{3/\rm yr} = 1.3 \times 10^{-21} \left(\frac{f_c}{1\ \rm kHz}\right) . \quad (53)$$

Combining equations (52) and (53) we find a ratio

$$\frac{h_c}{h_{3/\rm yr}} \approx 0.5 M_{1.4}^{3/2} R_{10}^{1/2} \left(\frac{r_0}{200\ \rm Mpc}\right)^{-1} . \quad (54)$$

where we have now used the distance $r_0 \sim 200$ Mpc within which mergers are expected to occur about three times per year (Narayan et al. 1991; Phinney 1991). Given the very approximate nature of this analysis, and the conservative estimate for r_0, the fact that $h_c/h_{3/\rm yr} \sim 1$ provides some encouragement that the final bursts of gravitational waves emitted by merging neutron stars should ultimately be detectable by LIGO.

We are very grateful to C. Evans for providing us his unpublished results for the gravitational radiation waveform of a head-on collision. Our work was supported by NSF grant AST 90-15451 and NASA grant NAGW-2364 to Cornell University. Computations were performed on the Cornell National Supercomputer Facility, a resource of the Center for Theory and Simulation in Science and Engineering at Cornell University, which receives major funding from the National Science Foundation and IBM Corporation, with additional support from New York State and members of its Corporate Research Institute.

REFERENCES

Abrahams, A., & Evans, C. R. 1992, in preparation
Abramovici, A., et al. 1992, Science, 256, 325
Anderson, S. B., Gorham, P. W., Kulkarni, S. R., Prince, T. A., & Wolszczan, A. 1990, Nature, 346, 42
Benz, W., Bowers, A. L., Cameron, A. G. W., & Press, W. H. 1990, ApJ, 348, 647
Boss, A. P., Cameron, A. G. W., & Benz, W. 1992, Icarus, in press
Centrella, J. M., Shapiro, S. L., Evans, C. R., Hawley, J. F., & Teukolsky, S. A. 1986, in Dynamical Spacetimes and Numerical Relativity, ed. J. M. Centrella (Cambridge: Cambridge Univ. Press), 238
Chandrasekhar, S. 1939, An Introduction to the Theory of Stellar Structure (Chicago: Univ. Chicago Press)
———. 1969, Ellipsoidal Figures of Equilibrium (New Haven: Yale Univ. Press)
———. 1975, ApJ, 202, 809
Clark, J. P. A., & Eardley, D. M. 1977, ApJ, 215, 311
Clark, J. P. A., van den Heuvel, E. P. J., & Sutantyo, W. 1979, A&A, 72, 120
Davies M., & Benz, W. 1991, ApJ, in press
Dyson, F. J. 1963, in Interstellar Communication, ed. A. G. W. Cameron (NY: Benjamin), 115
Evans, C. R. 1987, in Proc. of 13th Texas Symposium on Relativistic Astrophysics, ed. M. P. Ulmer (Singapore: World Scientific), 152
Evans, C. R., & Kochanek, C. S. 1989, ApJ, 346, L13
Evrard, A. E. 1988, MNRAS, 235, 911
Finn, L. S. 1989, in Frontiers of Numerical Relativity, ed. C. R. Evans, L. S. Finn, & D. W. Hobill (Cambridge: Cambridge Univ. Press), 126
Gilden, D. L., & Shapiro, S. L. 1984, ApJ, 287, 728
Gingold, R. A., & Monaghan, J. J. 1977, MNRAS, 181, 375
Harlow, F. H. 1988, Comput. Phys. Comm., 48, 1
Herant, M., & Benz, W. 1991, ApJ, in press
Hernquist, L., & Katz, N. 1989, ApJS, 70, 419
Hockney, R. W., & Eastwood, J. W. 1988, Computer Simulations Using Particles (Bristol: Adam Hilger)
Hulse, R. A., & Taylor, J. H. 1975, ApJ, 195, L51
Ipser, J., & Managan, M. 1981, ApJ, 256, 145
James, R. A. 1964, ApJ, 140, 552

Kochanek, C. S., Shapiro, S. L., Teukolsky, S. A., & Chernoff, D. F. 1990, ApJ, 358, 81
Kochanek, C. S., & Evans, C. R. 1989, in Frontiers of Numerical Relativity, ed. C. R. Evans, L. S. Finn, & D. W. Hobill (Cambridge: Cambridge Univ. Press), 297
Lai, D., Rasio, F. A., & Shapiro, S. L. 1992, in preparation
Lattanzio, J. C., Monaghan, J. J., Pongracic, H., & Schwarz, M. P. 1986, SIAM J. Sci. Stat. Comput., 7, 591
Lincoln, C. W., & Will, C. M. 1990, Phys. Rev. D, 42, 1123
Lucy, L. B. 1977, AJ, 82, 1013
Martin, P. G. 1970, Ap&SS, 7, 119
Misner, C. W., Thorne, K. S., & Wheeler, J. A. 1970, Gravitation (NY: Freeman)
Monaghan, J. J. 1985, Comput. Phys. Rep., 3, 71
———. 1989, J. Comput. Phys., 82, 1
Monaghan, J. J., & Lattanzio, J. C. 1985, A&A, 149, 135
———. 1991, ApJ, 375, 177
Monaghan, J. J., & Roxburgh, I. W. 1965, MNRAS, 131, 13
Nagasawa, M., Nakamura, T., & Miyama, S. M. 1988, PASJ, 40, 691
Nakamura, T., & Oohara, K. 1989, Prog. Theor. Phys., 82, 1066
Narayan, R., Piran, T., & Shemi, A. 1991, ApJ, 379, L17
Naylor, M. D. T., & Anand, S. P. S. 1970, in Stellar Rotation, ed. A. Slettebak (Dordrecht: Reidel), 163
Oohara, K., & Nakamura, T. 1989, Prog. Theor. Phys., 82, 535
———. 1990, Prog. Theor. Phys., 83, 906
Paczyński, B. 1990, ApJ, 348, 485
Phinney, E. S. 1991, ApJ, 380, L17
Quinlan, G., & Shapiro, S. L. 1989, ApJ, 346, 214
Rasio, F. A. 1991, Ph.D. thesis, Cornell Univ.
Rasio, F. A., & Shapiro, S. L. 1991, ApJ, 377, 559
———. 1992, in preparation
Schutz, B. F. 1986, Nature, 323, 310
———. 1989, In Gravitational Wave Data Analysis, ed. B. F. Schutz (Dordrecht: Kluwer), 3
Shapiro, S. L., & Teukolsky, S. A. 1983, Black Holes, White Dwarfs, and Neutron Stars (NY: Wiley)
Shapiro, P. R., Kang, H., & Villumsen, J. V. 1990, in Workshop on Large-Scale Structures and Peculiar Motions in the Universe, ed. D. W. Latham & L. N. da Costa (ASP Conference Series), 78
Stokes, G. H., Taylor, J. H., & Dewey, R. J. 1985, ApJ, 294, L21
Tassoul, J. L. 1978, Theory of Rotating Stars (Princeton: Princeton Univ. Press)
Tassoul, M. 1975, ApJ, 202, 803
Taylor, J. H., & Weisberg, J. M. 1989, ApJ, 345, 434
Thorne, K. S. 1987, in 300 Years of Gravitation, ed. S. Hawking & W. Israel (Cambridge: Cambridge Univ. Press), 378
Thorne, K. S. 1992, Phys. Rev. D, 45, 520
Vogt, R. E. 1992, in Proc. of the 6th Marcel Grossman Meeting on General Relativity, in press
Wells, N. H., Burrus, C. S., Desobry, G. E., & Boyer, A. L. 1990, Comput. Phys., 4, 507
Wolszczan, A. 1991, Nature, 350, 688
Wood, D. 1981, MNRAS, 194, 201
———. 1982, MNRAS, 199, 331